The Meteoritical Society

Meteoritics & Planetary Science 50, Nr 1, 141–171 (2015)
doi: 10.1111/maps.12408

The distribution of megablocks in the Ries crater, Germany: Remote sensing, field investigation, and statistical analyses

Sebastian STURM[1*], Thomas KENKMANN[1], Malte WILLMES[2], Gisela PÖSGES[3], and Harald HIESINGER[4]

[1]Institute of Earth and Environmental Sciences—Geology, Albert-Ludwigs-Universität Freiburg (ALU), Albertstr. 23-B, D-79104 Freiburg, Germany
[2]Research School of Earth Sciences, Australian National University (ANU), 142 Mills Road, Acton, Canberra 0200, Australia
[3]Rieskrater Museum, Eugene-Shoemaker-Platz 1, D-86720 Nördlingen, Germany
[4]Institut für Planetologie, Westfälische Wilhelms-Universität Münster (WWU), Wilhelm-Klemm-Straße 10, D-48149 Münster, Germany
[*]Corresponding author. E-mail: sebastian.sturm@geologie.uni-freiburg.de

(Received 03 December 2013; revision accepted 04 November 2014)

Abstract–The Ries crater is a well-preserved, complex impact crater that has been extensively used in the study of impact crater formation processes across the solar system. However, its geologic structure, especially the megablock zone, still poses questions regarding crater formation mechanics. The megablock zone, located between the inner crystalline ring and outer, morphologic crater rim, consists of allochthonous crystalline and sedimentary blocks, Bunte Breccia deposits, patches of suevite, and parautochthonous sedimentary blocks that slumped into the crater during crater modification. Our remote sensing detection method in combination with a shallow drilling campaign and geoelectric measurements at two selected megablocks proved successful in finding new megablock structures (>25 m mean diameter) within the upper approximately 1.5 m of the subsurface in the megablock zone. We analyzed 1777 megablocks of the megablock zone, 81 of which are new discoveries. In our statistical analysis, we also included 2318 ejecta blocks >25 m beyond the crater rim. Parautochthonous megablocks show an increase in total area and size toward the final crater rim. The sizes of allochthonous megablocks generally decrease with increasing radial range, but inside the megablock zone, the coverage with postimpact sediments obscures this trend. The size-frequency distribution of all megablocks obeys a power-law distribution with an exponent between approximately −1.7 and −2.3. We estimated a total volume of 95 km^3 of Bunte Breccia and 47 km^3 of megablocks. Ejecta volume calculations and a palinspastic restoration of the extension within the megablock zone indicate that the transient cavity diameter was probably 14–15 km.

INTRODUCTION

Impact crater formation represents a fundamental geologic process. The information gained from the investigation of terrestrial impact structures and those formed on other bodies in the solar system is complementary. Terrestrial structures—rarely preserved morphologically—allow the sampling of rocks, provide subsurface data, and yield information about impact-related structural, petrological, petrophysical, and geochemical modifications (e.g., Grieve 1987; Melosh 1989; French 1998; Kenkmann et al. 2014). Remote sensing studies of pristine structures on other bodies provide mainly morphologic data. In this context, the Ries is a rare exception and of special interest, because it represents a well-preserved and only weakly eroded complex crater on Earth that is easily accessed and that provides ground truth for the proposed models of impact crater formation. Given the well-documented preimpact geology of the Ries, the distribution of megablocks (>25 m) contains information about the impact process itself and postimpact modifications. For

© The Meteoritical Society, 2014.

this study, we combined remote sensing data and field work (e.g., Sturm 2011; Willmes 2011) to revise and complete the distribution of megablocks by Hüttner and Schmidt-Kaler (1999) within and outside of the crater. The provenance, lithology, size, and shape preferred orientation of megablocks are statistically investigated with respect to their location in the crater. Objectives of this study are the detection of new megablock structures by means of high-resolution airborne images (Sturm 2011; Willmes 2011), refinement of previous mappings by geophysical and airborne data, and a rigorous spatial and statistical analysis of all megablocks of the Ries crater to derive fundamental information about the excavation process and the dynamic fragmentation of rocks.

Geologic Setting of the Ries Crater, Germany

The Ries crater, located in southern Germany (48°52′38.02″N/10°32′56.38″E), has a diameter of approximately 26 km and is classified as a complex impact crater. It cuts into the Schwäbisch-Fränkische Alb, a WSW–ENE-trending major escarpment in southern Germany that was already present at the time of impact (Graup 1999). Consequently, the southern crater rim is about 150 m higher than the northern rim. Confirmed as an impact crater by Shoemaker and Chao (1961), the complex geologic history of the Ries impact has been intensively studied by means of geological, geophysical, and geochronologic methods, as well as numerical modeling (e.g., Pohl and Gall 1977; Pohl et al. 1977; Stöffler 1977; Hörz et al. 1983; Von Engelhardt 1990; Stöffler et al. 2002; Osinski et al. 2004; Wünnemann et al. 2005; Kenkmann and Ivanov 2006; Collins et al. 2008; Buchner et al. 2010; Stöffler et al. 2013; Sturm et al. 2013). Taking into account all available K/Ar and ^{40}Ar-^{39}Ar age data from the literature (e.g., Buchner et al. 2003; Laurenzi et al. 2003; Di Vincenzo and Skala 2009), a best age value for the Ries impact event of 14.9 Ma was suggested by Rocholl et al. (2011).

The geologic history of the Ries can be divided into preimpact, impact, and postimpact stages (e.g., Bayerisches Geologisches Landesamt 1969, 1974, 1977), reviewed in detail by Von Engelhardt (1990) and summarized by Hüttner and Schmidt-Kaler (1999) in the description of the 1:50,000 scale geologic map of the Ries (Hüttner and Schmidt-Kaler 1999).

Preimpact Geology

The Ries impact occurred in 650–750 m thick well-stratified sediments of Triassic to Neogene age underlain by crystalline basement rocks. The crystalline basement consists predominantly of pre-Variscan metamorphic rocks (orthogneisses, paragneisses, metabasites) with Variscan intrusive magmatites (especially granites) that belong to the Moldanubian zone of the Variscan orogeny (e.g., Stettner 1974; Graup 1975, 1977). The overlying Triassic sediments are made up of about 50 m of Muschelkalk (Mid-Triassic) and 200 m thick coarse-grained sandstones and red mudstones of the Keuper sequence (Upper Triassic) (Hüttner and Schmidt-Kaler 1999). They are overlain by Jurassic sediments, which consist of 30 m of interlayered sandstone, mud- and claystone deposits of Liassic age, followed by 140 m iron-rich sandstones of Dogger age and a 200 m thick Malmian limestone sequence (Hüttner and Schmidt-Kaler 1999). During the Cretaceous, the Jurassic limestones underwent deep erosion and karstification. This erosion of the sedimentary units continued also in the Neogene (Hüttner and Schmidt-Kaler 1999). During the upper Miocene, the southern part of the Ries became a distal part of the foredeep of the northward propagating Alpine orogeny, the so-called Molasse basin. The deposits of the Upper Marine Molasse (OMM) transgressed the outliers of the Ries area, and during the middle Miocene, the Upper Freshwater Molasse (OSM) reached into the future crater region, depositing mica-rich sands and shales. The landscape before the impact was dominated by the Jurassic WSW–ENE-trending escarpment of Malmian limestone that dissected the future target area (Hüttner and Schmidt-Kaler 1999).

The Ries Crater and Its Impactites

The projectile that created the Ries crater was about 1000–1500 m in diameter, traveling most likely at a speed of 20–50 km s^{-1} (Stöffler et al. 2002). The formation of the Ries crater is closely related to the formation of the Steinheim basin, which was formed at the same time (Stöffler et al. 2002). Modeling results (Stöffler et al. 2002) show that an oblique impact of a binary asteroid from the WSW with an angle of 30–50° best explains the location of the craters and the distribution of their distal ejecta. The Ries has a deep central basin with a diameter of approximately 12–13 km, bounded by a hummocky inner ring that is surrounded by a 7–8 km wide annulus called the megablock zone, and the outer crater rim (Fig. 1) (Hüttner and Schmidt-Kaler 1999). This outer rim forms a topographic high and is defined by concentric normal faults that separate the surrounding autochthonous units from the parautochthonous megablocks that were down-faulted (Hüttner and Schmidt-Kaler 1999).

The inner ring consists of uplifted crystalline basement rocks that are partly covered by postimpact

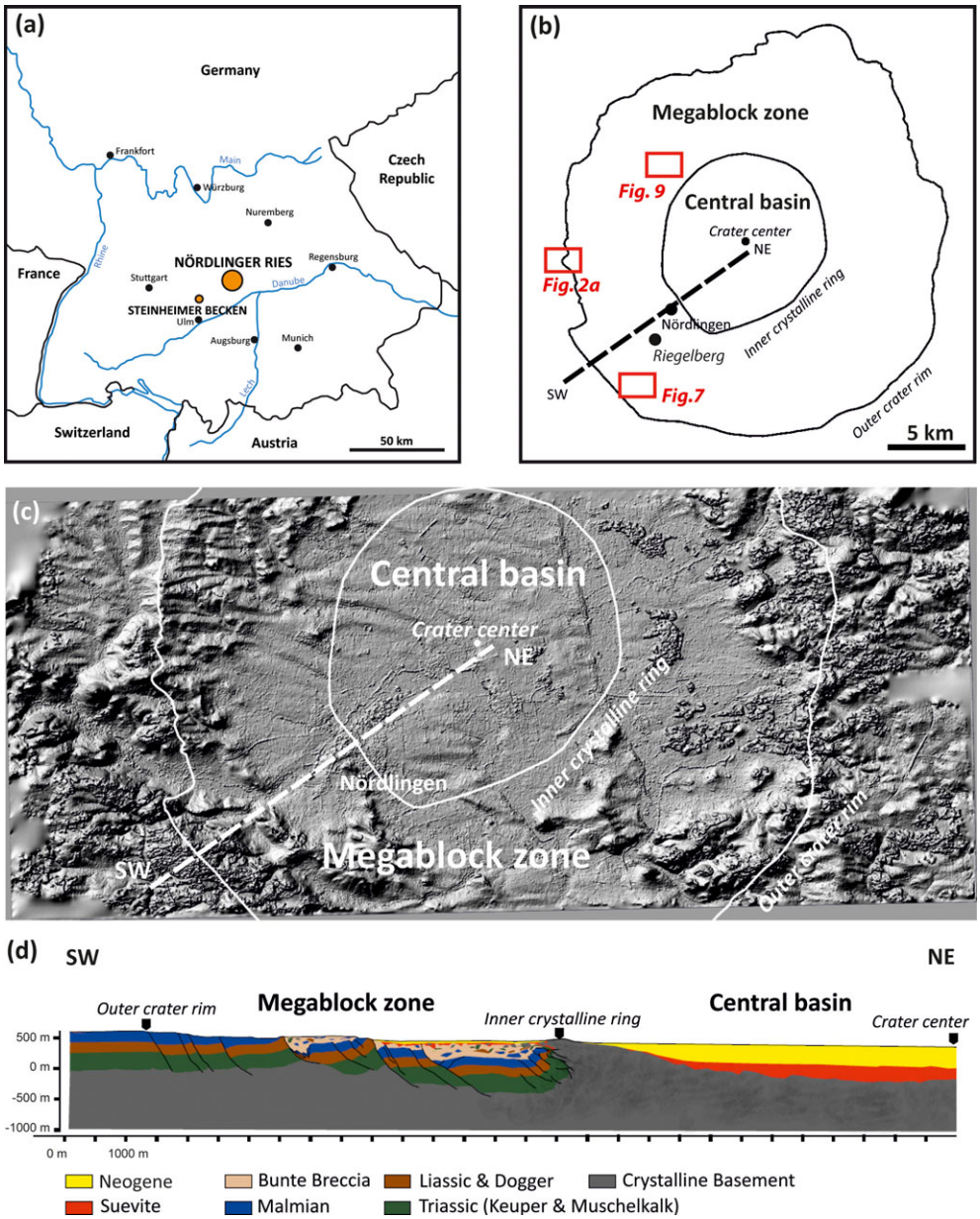

Fig. 1. a) Geographic location of the Ries crater, b) overview map showing the crater structure, c) high-resolution Digital Elevation Model (DEM), and d) cross section of the Ries crater; the location of the profile is shown in (b) and (c) as dashed lines (modified after Collins et al. 2008).

Ries lake sediments (e.g., the Wallerstein hill; Hüttner and Schmidt-Kaler 1999). It is believed that this inner ring closely corresponds to the rim of the transient cavity that developed during the excavation stage of crater formation (Wünnemann et al. 2005). This central cavity has a bowl shape, whose floor formed in uplifted crystalline basement about 600 m below the current surface level (Stöffler 1977). The cavity is filled by approximately 300 m of suevite and postimpact lake deposits of 200–400 m thickness (Ernstson 1974). The research borehole Nördlingen 1973 provides a profile through the shattered crater floor, suevite, and lake deposits (Bayerisches Geologisches Landesamt 1974; Stöffler 1977).

The impactites of the Ries crater have been classified based on their composition, size of components, and shock-metamorphic level by Hüttner (1969). They can be subdivided into polymict and monomict crystalline breccias, outer- and crater suevites, polymict and monomict sedimentary breccias, and Ries tektites (moldavites) as distal ejecta (Gall et al. 1977; Von Engelhardt 1990; Hüttner and Schmidt-Kaler

1999; Stöffler et al. 2013). The term Bunte Trümmermassen is used here synonymous with the deposits of the continuous ejecta blanket and includes the entity of Bunte Breccia plus those allochthonous megablocks which originate in the transient cavity (Hüttner and Schmidt-Kaler 1999). The most widespread impact unit is the Bunte Breccia deposit (Von Engelhardt et al. 1969; Hüttner 1969; Schneider 1971). This polymict breccia consists of rock and mineral fragments derived predominantly from the overlying sedimentary cover and to a lesser amount from the crystalline basement. Bunte Breccia contains 3–10% lithic clasts (especially crystalline rock fragments) that can show shock levels up to about 35 GPa (Pohl et al. 1977; Stöffler and Ostertag 1983; Von Engelhardt 1990). With increasing radial range, more and more reworked local surface material (e.g., Upper Marine Molasse and Upper Freshwater Molasse sediments) was incorporated outside the final crater (Hörz et al. 1983; Von Engelhardt 1990).

The present-day asymmetric distribution of Bunte Trümmermassen (Hüttner and Schmidt-Kaler 1999), extending farther to the south and to the east than to the north and west, is most likely the result of selective erosion that removed in particular the northern ejecta blanket (Von Engelhardt 1990). The Bunte Breccia deposits extend up to four crater radii from the impact center. Most recent interpolation results of the Bunte Trümmermassen and Bunte Breccia deposits outside the Ries crater by Sturm et al. (2013) show that their total thickness deviates from a steady decrease with radial range which was postulated for the primary ejecta distribution (McGetchin et al. 1973; Hörz et al. 1983). Sturm et al. (2013) found a depression (called moat) followed by a ridge (called rampart) of thick Bunte Breccia at approximately two crater radii from the crater center. Bunte Breccia deposits also cover the megablock zone, but are absent inside the central basin suggesting this area was indeed the transient crater cavity. Bunte Trümmermassen was also affected by motion related to crater modification. Subsequent to their deposition from the ejecta curtain, they moved downward and inward, and created a complex juxtaposition of different rock units between the inner and outer rim (Hüttner and Schmidt-Kaler 1999).

Postimpact Geologic History

The impact changed the surrounding area dramatically by displacing large amounts of material, which clogged the pre-existing fluvial valleys. Many lakes developed, the biggest one being the Rezat-Altmühl Lake, comparable in size to the present-day Lake Constance, caused by the ponding of the Ur-Main. Within the crater, the Ries Lake formed and existed for approximately 2 Ma (Hüttner and Schmidt-Kaler 1999; Arp 2006), depositing sediments approximately 300 m thick. Multiple river systems developed on the crater floor that partially followed the preimpact river systems. During the Miocene, the Rezat-Altmühl Lake was filled with sediments deposited by the ancient Main, covering parts of the proximal ejecta in the NE with sand deposits. The Ries crater and parts of its ejecta blanket were, thus, covered with terrestrial sediments, which fortunately most of the original impact region, until the area was uplifted and exhumed much later during the Pleistocene. This extended time of burial led to the good preservation of the Ries crater and its impact formations (e.g., Gall et al. 1975; Füchtbauer et al. 1977). The relief observed today was formed during the Pleistocene ice ages and is the result of erosional processes, valley formation, and karstification. The Wörnitz and Eger rivers—discharging today from the Ries depression to the SE—partially removed the Ries Lake clays and mudstones from the central basin, leaving behind the more resistant Ries Lake limestones. In the western and northern part of the crater, the morphologic crater rim has been degraded by postimpact erosion leading to the current topography of the crater (Hüttner and Schmidt-Kaler 1999).

Megablocks

We define megablocks as coherent, lithologically homogenous blocks of rock larger than 25 m that were displaced and partly brecciated during crater formation (Pohl et al. 1977). Field mapping generally delineated such blocks individually and assigned all smaller materials to the otherwise undifferentiated "Bunte Trümmermassen" (see below). Megablocks can be generated during different stages of the crater formation that overlap in time. Three types of megablocks can be distinguished. (1) Megablocks that are ejected during the excavation stage and deposited beyond the final crater rim as part of the continuous ejecta blanket (Bunte Trümmermassen) outside of the crater. (2) Megablocks that are ejected during the excavation stage and deposited inside the final crater rim, but outside the inner crystalline ring (=transient cavity rim). These megablocks are likewise part of the continuous ejecta blanket (Bunte Trümmermassen), but were deposited on a surface that was subject to inward and downward movements during subsequent gravity-driven crater modification. (3) Megablocks that are not ejected, but that represent slumped blocks that moved gravitationally downward and inward into the crater cavity during the modification stage. Type I occurs only outside the final crater rim, whereas types II and III are

restricted to the megablock zone sensu strictu. In addition, megablocks consisting of local substrate can be formed by secondary cratering processes outside the crater structure (e.g., Upper Freshwater Molasse or Upper Seawater Molasse). Types I and II are termed *allochthonous megablocks* and are defined as blocks that have been thrown out or moved over considerable distances, and were typically embedded into fine-grained breccia matrix (called Bunte Breccia). Together with Bunte Breccia, they form the Bunte Trümmermassen. Type III, termed *parautochthonous megablocks*, were deformed by moderate to minor displacements during crater collapse. They are typically bounded by discrete fault zones and are not underlain by Bunte Breccia (Von Engelhardt 1990; Hüttner and Schmidt-Kaler 1999). Parautochthonous megablocks usually show no indication of shock deformation, whereas allochthonous megablocks can show different shock-metamorphic stages, e.g., the crystalline megablocks (Abadian 1972). In general, parautochthonous megablocks are less deformed than their allochthonous counterparts and are found close to the crater rim. It is especially these massive blocks that lead to the recognition of a "megablock zone" at the Ries, i.e., to an annulus of generally large blocks just inside the morphological, 26 km diameter, rim.

At the Ries crater, megablocks originated from all preimpact lithologies (crystalline basement, Malmian, Dogger, Liassic, and Keuper), with Malmian limestones and crystalline megablocks being the dominant lithologies (Von Engelhardt 1990; Hüttner and Schmidt-Kaler 1999).

Crystalline megablocks are, in principle, allochthonous, as they originate from the deep-seated crystalline basement and were thrown out during the excavation phase. The hills that sporadically outline the inner crater ring are presumably built up of clusters of crystalline megablocks. These blocks represent the innermost, most proximal part of the ejecta blanket that delineates the transient crater cavity (Wünnemann et al. 2005). Recently, in the Erbisberg drill core (48°49′51.60″ N/10°30′43.14″E), obtained southeast of Nördlingen on the southern crystalline ring, Kruppa (2013) and Wilk (2014) described a polymict crystalline breccia that consists of three different bedrock units (1) a partial pegmatitic gneiss, (2) a hornblende gneiss, and (3) a biotite–plagioclase-rich gneiss. This polymict crystalline breccia sequence is underlain by red and white Keuper sandstones (Arp et al. 2011; Jung et al. 2011). Large ejected crystalline megablocks are also found in the megablock zone between the inner and outer crater rims, but also occur beyond the outer rim in restricted radial, ray-like zones (Graup 1975). Detailed insights into crystalline megablocks are provided by examples near Unterwilflingen (48°54′45.20″N/10°25′5.99″E) and Wengenhausen (48°54′40″N/10°27′46″E). These two occurrences consist predominantly of highly weathered granites and gneisses, and represent rotated allochthonous crystalline megablocks (Hüttner and Schmidt-Kaler 1999).

Like all the Bunte Trümmermassen, the ejected crystalline blocks show an asymmetric distribution outside the crater rim with a concentration in the southern regions near the morphologic crater rim (Von Engelhardt 1990). Malmian megablocks are often intensely brecciated down to microscopic scales and represent "monomict breccias" (Hüttner 1969). With a length of up to 1.75 km, the Riegelberg (48°49′05″N/ 10°27′02″E), consisting of Malmian limestone, represents the largest known megablock structure in the megablock zone of the Ries crater.

METHODS

A systematic survey of the megablock zone was performed with a combined approach of remote sensing and field work including geologic mapping, shallow drilling, and geoelectric resistivity measurements. In addition, all megablocks, including those beyond the outer rim, from the recent geologic map 1:50,000 (Hüttner and Schmidt-Kaler 1999) were digitized and included in this GIS-project to obtain quantitative data on the distribution, size, lithology, deformation, and volume of all megablocks of the Ries impact crater.

Detection of Megablocks

The method to unveil features hidden in the subsurface is well known from aerial archeology (e.g., Brophy and Cowley 2005) and for example, from the mapping of paleopermafrost features in Skåne, southern Sweden (Svensson 1973). The basic principle behind the remote detection of megablocks is based on the fact that these structures have lithological and physical characteristics that differ from their surroundings. Megablocks with surface outcrops often form a hummocky relief and show a typical vegetation cover consisting of juniper bushes and calcareous, low-nutrient, brown grassland (Fig. 2). In addition, due to low water storage in these fractured megablocks, they are mostly not used for agriculture and can, thus, be distinguished from the surrounding, more fertile fields. The detection of megablocks in the subsurface with a few meters of topsoil cover is based on the same principles. Due to the fracture-induced high permeability and lithology of the megablocks, the soil cover on top has a different moisture level than the surrounding soil. In the field and on aerial images,

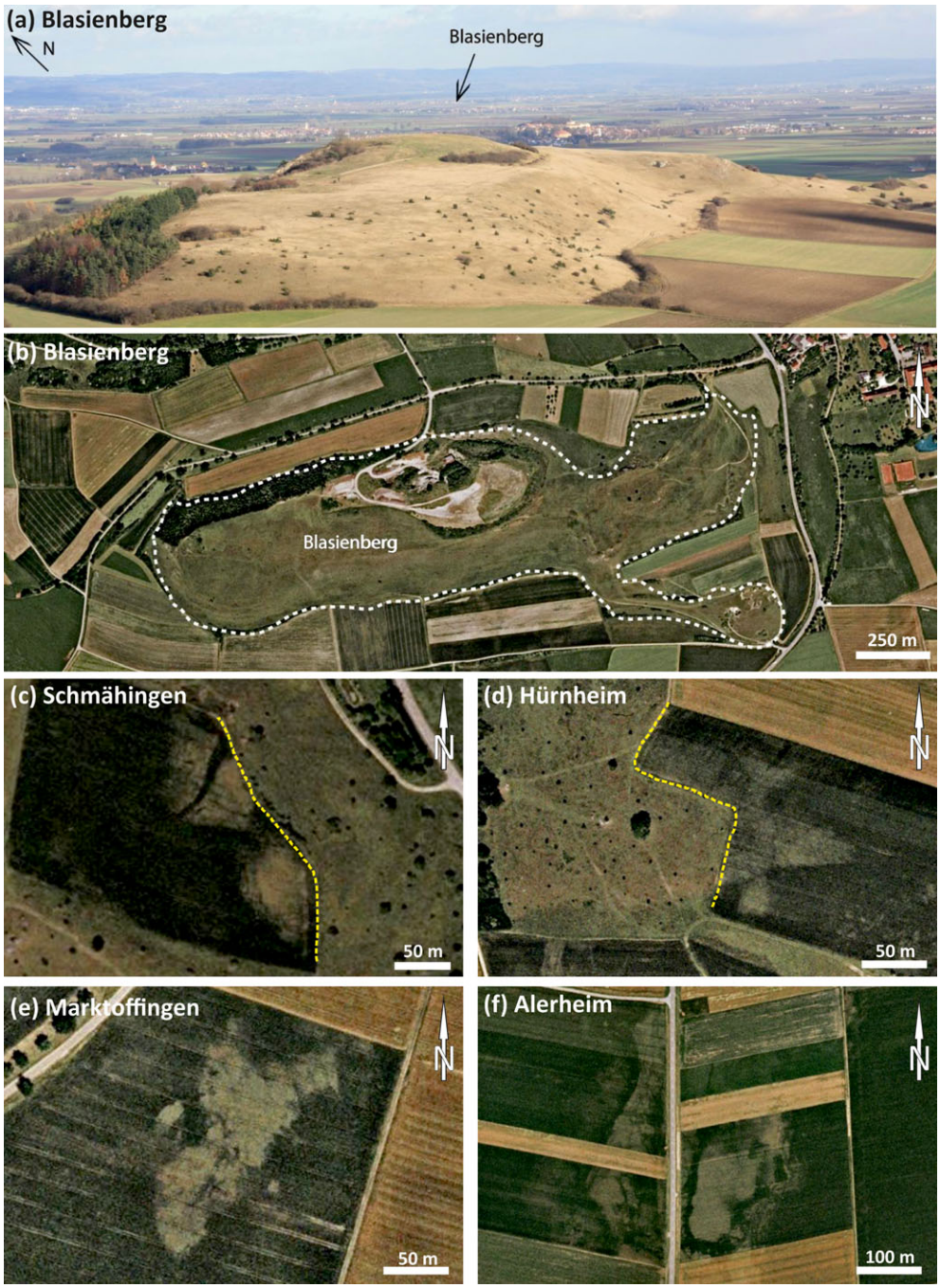

Fig. 2. a) The Blasienberg (48°52′29N/10°22′59″E) Ries, a Malmian limestone megablock exposed at surface (location shown in Fig. 1), and (b–d) examples of surface megablocks visible in Google Earth images (yellow dashed line represents the boundary between surface and subsurface megablocks) (Blasienberg—48°52′29N/10°22′59″E, Schmähingen—48°48′34.39″N/10°30′47.66″E, Hürnheim—48°48′15.16″N/10°29′48.52″E). e–f) Google Earth images showing examples of the visibility of subsurface megablocks in the fields (Marktoffingen—48°56′1.57″N/10°28′39.13″E, Alerheim—48°49′55.21″N/10°37′21.72″E).

megablocks show up as high-albedo features that have no, or only sparse, vegetation. The method cannot be applied to forested areas that cover less than approximately 5% of the megablock zone between inner and outer rim: our efforts to detect additional, hitherto unmapped, megablocks were confined to this annulus.

Data Sets

High-resolution aerial images obtained by different cameras at different times were used to investigate the megablock zone. These include aerial images from GeoContent available through Google Earth, High-

Resolution Stereo Camera Airborne (HRSC-AX) images, and a Digital Elevation Model (DEM) derived from the Advanced Spaceborne Thermal Emission and Reflection Radiometer (ASTER) and HRSC-AX data sets.

Aerial Images from Google Earth

The highest resolution images of Google Earth available had a spatial resolution of approximately 0.5 m and were acquired by GeoContent in April 2001. Images, each covering an area of 301 × 220 m with an overlap of 30% at an observation altitude of 727 m, were extracted from Google Earth. These images were then stitched together to an image mosaic with a resolution of approximately 1 m of the crater interior in a multistep process using Adobe Photoshop CS3 (Adobe), georeferenced and imported into ArcGIS (ESRI).

HRSC-AX

The HRSC airborne imaging system combined with its photogrammetric processing software allows the production of digital image data at very high spatial resolution, very high positional accuracy, and high radiometric resolution (Neukum et al. 2001; Scholten and Gwinner 2004). HRSC-AX is a multispectral, multistereo camera that produces ortho-images and digital surface models with an accuracy of 10–20 cm from an altitude of approximately 2500 m (Neukum et al. 2001; Scholten and Gwinner 2004). Four different data products were available; pan-chromatic images (PAN), truecolor images (RGB), colored infrared images (CIR), and a Digital Elevation Model (DEM). Relative accuracies are in the range of approximately 5 cm. The absolute spatial accuracy is approximately 15–20 cm, and the absolute height accuracy is 20–25 cm, both compared to the WGS84 reference system (Neukum et al. 2001). The coverage of HRSC-AX images acquired in April 2009 of the Ries is approximately 400 km^2, or approximately 75% of the entire impact structure. The northernmost and southernmost parts of the megablock zone as well as the outer crater rim in those regions are not covered by the HRSC-AX data. The image processing was performed in 2010 at the DLR in Berlin. In addition, a Digital Elevation Model (DEM) with a spatial resolution of approximately 1 m (Fig. 1c) was compiled, a significant improvement over the previously available ASTER DEM of approximately 30 m.

Shallow Drilling

In total, 122 sites were drilled (0–5 m depth) to confirm suspected megablock structures and to determine their lithologies. In addition, for many previously known megablocks, their shape was better constrained and their lithologies verified. Drilling was performed at selected locations in conjunction with geologic mapping to investigate the lithology and depth of subsurface megablocks. Two different types of drilling equipment (Pürckhauer and percussion piston corer) were used during the field campaign. Both produced similar results. The lithology and grain size for each drilling profile was recorded in the field and grain size distributions were characterized based on the German standard DIN4022. The data were imported into the drill core software GGU-STRATIG (GGU-Software), which was used to draw the drill profiles according to DIN4023 (DIN—German Institute for Standardization).

Table 1. Specific resistivities of rocks and different grain sizes used in this study (Knödel et al. 2005).

	Resistivity values (Ωm)	
Material	Minimum	Maximum
Gravel	50 (water saturated)	$>10^4$ (dry)
Sand	50 (water saturated)	$>10^4$ (dry)
Silt	20	50
Clay	3	30
Soil (mixture of sand, silt, and clay)	3	$>10^4$ (only 100% dry sand content)
Sandstone	<50 (wet)	$>10^5$ (compact)
Limestone	100 (wet)	$>10^5$ (compact)
Magmatitic, metamorphic	150 (weathered, wet)	$>10^6$ (compact)

Geoelectric Measurements

We used geoelectrical measurements to identify and study in detail two selected megablocks. The method is based on an induced electric current causing an apparent resistivity for distinct geologic layers in the subsurface. The inversion program RES2DINV for 2-D tomographic models was used to calculate the measured profile sections. The measured apparent resistivity is a volume-correlated value which is converted with an inversion program to model the subsurface geology (Griffiths and Barker 1993). The geologic model yields the observed distribution of the apparent resistivity values. The data inversion produces a 2-D image (called tomograph) that shows the distribution of the true resistivity values of the subsurface layer material. Different specific resistivity values allow us to determine different material structures in the subsurface (Table 1). However, to constrain the model, ground truth data from borehole profiles are necessary (Assaad et al. 2004). We used a geoelectric setup consisting of a linear array of multiple electrodes on the ground surface. Four electrodes, two current and two measurement electrodes, were automatically selected by computerized

instruments (e.g., Geotom Mk-RES/IP/SP). This enables the collection of multiple data points in a short period of time. The current and measurement electrode can be arranged in different configurations (e.g., Schlumberger, Wenner, pole–dipole, or dipole–dipole). Employing a Wenner array configuration with 1 m and/or 2 m spacings between each electrode, we were able to detect two subsurface megablock structures (1) a Malmian limestone megablock near Hürnheim and (2) a crystalline megablock near Marktoffingen. Topographic data were incorporated into the program RES2DINV and the resulting cross sections were adjusted producing the final 2-D tomography. The collected data were then processed with the computer program RES2DINV with a derived *Abs error* that represents the root mean square error between the observed apparent resistivity data and the modeled one.

Mapping

To generate a coherent map of the megablock zone and the ejecta blanket outside the Ries crater, all available data sets, including airborne and satellite images, digital terrain models (DTM), the geologic map of the Ries, and findings from the field campaign were imported into an ArcGIS (ESRI) project and analyzed in a multistep process. A systematic survey of the megablock zone was performed and all observable surface and subsurface megablocks were mapped. The megablocks from the geologic map and the megablocks found in our survey were merged using the Editor Tool from ArcGIS (ESRI). Megablocks were classified based on their stratigraphy and mode of displacement into 10 groups, with parautochthonous essentially synonymous with slumping, and allochthonous implying ballistic deposition (1) Malmian parautochthonous, (2) Malmian allochthonous, (3) Dogger parautochthonous, (4) Dogger allochthonous, (5) Liassic parautochthonous, (6) Liassic allochthonous, (7) Keuper parautochthonous, (8) Keuper allochthonous, (9) crystalline basement allochthonous, and (10) megablocks of unknown stratigraphic provenance. The minimum size of 25 m of megablocks usually assured sufficient lithological characteristics to unambiguously assign each block to a specific stratigraphy. A further subdivision of the stratigraphy could not be carried out.

The classification of subsurface megablocks was limited to locations where drilling was possible and/or where fieldstones had been mapped before. With the available data, it is not possible to distinguish between allochthonous and parautochthonous megablocks in the subsurface. For subsurface blocks located immediately adjacent to previously mapped megablocks, we assumed that both blocks are of the same lithology and depositional history. For example, a newly discovered Malmian limestone megablock located next to an already mapped and classified as "allochthonous" Malmian megablock would also be assigned allochthonous. In cases where the new block was isolated, but relatively close to other allochthonous blocks, it was also mapped as allochthonous. We classified subsurface features with unknown lithology or stratigraphy data, that show similar albedo characteristics like verified buried megablocks, as megablocks of unknown stratigraphic provenance. These megablocks of uncertain stratigraphy are excluded from further statistical analysis, as this class most likely contains megablocks from several different lithologies and types of transportation.

Data and Statistical Analyses

Megablocks were analyzed with respect to their distance to crater center, their size, and volumes:

Distance to Crater Center

The center point for each megablock was determined using the "Vector Editing" tool from the Hawth's tool plugin (Spatialecology) for ArcGIS (ESRI) to determine the distance of the megablocks to the crater center. The "Analysis" tool was used to determine the distance from the center point of each megablock to the crater center.

Size and Size Distribution of Megablocks

The area for each megablock was calculated using the "Calculate Geometry" function of ArcGIS (ESRI). The block size was derived using the "Minimum Boundary Geometry" function of ArcGIS (ESRI). The function derives the length (x-value) and width (y-value) of each megablock in plane view. First, an equivalent area circle was calculated from the mapped area on the surface. From the equivalent radius, the diameter was calculated and taken as the block size "b" of each megablock.

For each type of megablock (e.g., parautochthonous Keuper), the block size distribution was displayed in a cumulative double logarithmic frequency diagram. This is reasonable, as the size distribution of fragmented rock can usually be described by a power-law relationship (e.g., Sammis et al. 1987) given as:

$$N(>d) = Cd^{-D} \tag{1}$$

where $N(>d)$ is the number of blocks larger than the diameter d, C is a constant, and D is the power-law exponent characterizing the distribution.

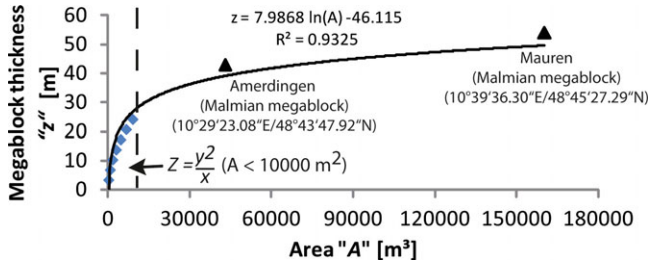

Fig. 3. Area "A" versus the calculated megablock thickness "z." For megablocks with an area smaller than 10,000 m^2, we used the assumption "$z = y^2/x$" (x = length, y = width, z = depth). For megablocks with an area larger than 10,000 m^2, we used two drill sites into limestone megablocks (at Amerdingen and Mauren; outside of the crater) of known thickness to fix and finally derive a power law (black line) for the depth (z-value) of each megablock.

Megablock Thickness (z-value)

For small-to-moderately sized megablocks, we estimated the thickness of megablocks by the equation:

$$z = \frac{y^2}{x} (A < 10,000\,\mathrm{m}^2) \tag{2}$$

where x, y, and z are the length, width, and depth of the block. For block sizes with a plane-view area larger than 10,000 m², we adopted the ratios of thickness to the horizontal dimensions from two megablocks whose 3rd dimension was known from drilling (Mauren—10°29′23.08″E/48°43′47.92″N, Amerdingen—10°39′36.30″E/48°45′27.29″) (Fig. 3). Combining Equation 2 and these data sets, we derived an equation for determining the megablock thickness (z-value):

$$z = 7.9868 \ln(A) - 46.115 \tag{3}$$

Volumes of "Bunte Trümmermassen," Allochthonous Megablocks, and Bunte Breccia

Megablock Zone

We used the geologic cross section constructed by Collins et al. (2008) to determine the area and volume of Bunte Trümmermassen "V_{BT}" of the megablock zone. As defined earlier, Bunte Trümmermassen represents the combined deposits of the ejecta blanket and is the sum of the volumes of allochthonous megablocks "V_{MB}" and Bunte Breccia matrix "V_{BB}";

$$V_{BT\_in} = V_{MB\_in} + V_{BB\_in} \tag{4}$$

The suffixes "$_{in}$" and "$_{out}$" stand for measurements inside and outside the morphologic crater rim, respectively. To determine "V_{BT}," the cross section of Collins et al. (2008) (Fig. 4) was subdivided into four parts (1–4); each of them is regarded to have constant thicknesses of Bunte Trümmermassen. Assuming axial symmetry "V_{BT_in}" is given by:

$$V_{BTin} \sum_{i=1-4} \pi r_{i+1}^2 t_{BT(i+1)} - \pi r_i^2 t_{BT(i+1)} \tag{5}$$

To calculate "V_{MB}," the total volume of megablocks of the megablock zone, the volume of each megablock was determined using the equivalent ellipsoid volume of each single megablock with axes x, y, and z:

$$V_{MB} = \sum V_{MBsingle} = \sum \frac{1}{6} \pi xyz \tag{6}$$

Megablocks could be identified only at the surface and in the shallow subsurface. To estimate the volumetric fraction of megablocks over the full depth of the Bunte Trümmermassen (Table 2), we assumed that the near-surface megablocks in the southwestern megablock zone, where the cross section of Collins et al. (2008) is trending to, show a typical megablock distribution that remained constant over the entire thickness of the Bunte Trümmermassen. We multiplied each megablock by a factor "s," which is the ratio of the Bunte Trümmermassen thickness obtained from the cross section and the z-value of each megablock:

$$s = \frac{t_{BT}}{z} * 2 \tag{7}$$

The volume of Bunte Breccia "V_{BB_in}" is determined from the "V_{BT_in}" and "V_{MB_in}" using Equation 4.

Table 2. Classification of the megablock zone as derived with the information from Collins et al. (2008); all dimensions are in meters.

Region inside the crater	Radius "r" derived after Collins et al. (2008) (Fig. 4)	Bunte Trümmermassen thickness "t_{BT_in}"
1	8500	300
2	9500	180
3	11,000	200
4	>11,000	60

Volume of the Ejecta Blanket Outside the Crater Rim

We subdivided the zone beyond the crater rim into three regions (Table 3; Fig. 5) with different average

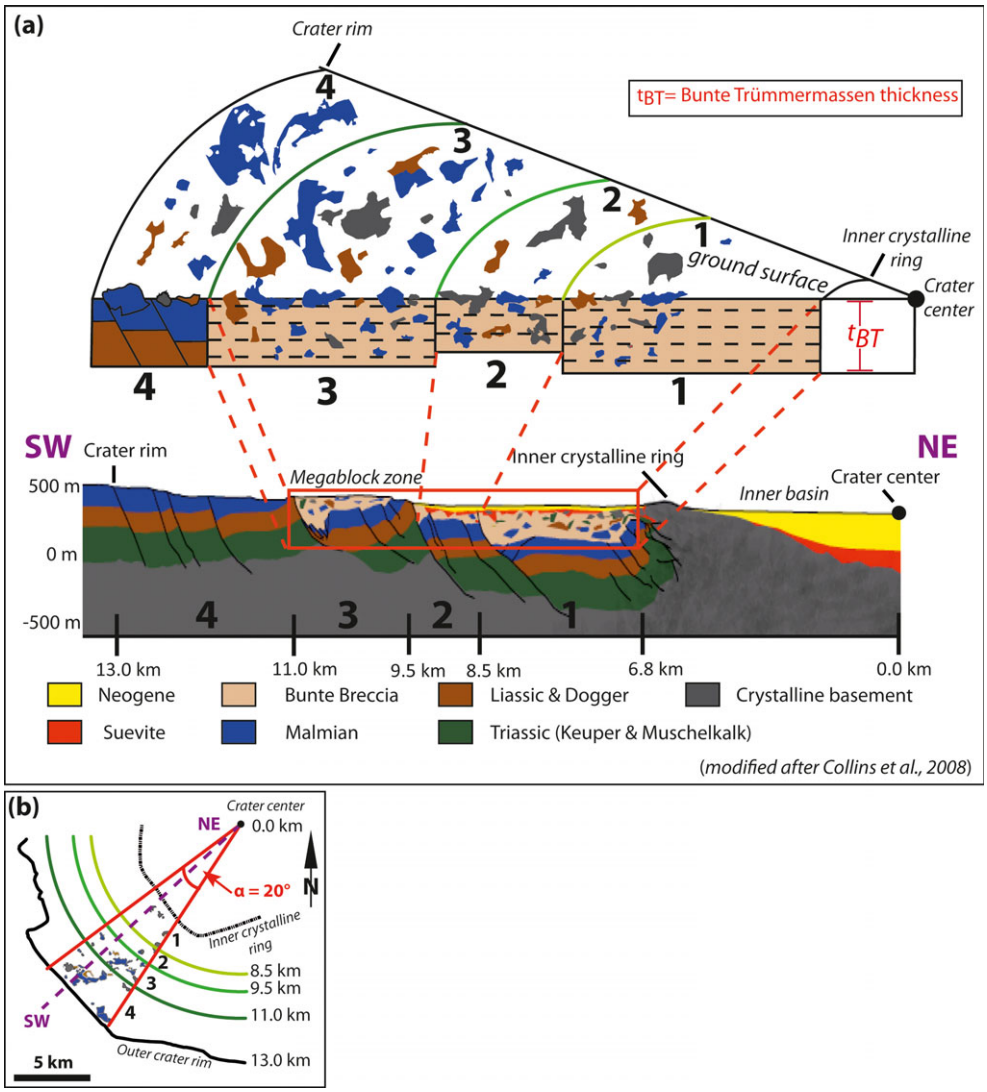

Fig. 4. a) Sketch illustrating the volume calculations for megablocks and Bunte Trümmermassen of the megablock zone utilizing a modified cross section (SW–NE) after Collins et al. (2008). The megablock zone is subdivided into four regions with specific Bunte Trümmermassen thicknesses "t_{BT}" from the inner crystalline ring to the final crater rim. Bunte Trümmermassen thicknesses "t_{BT}" are derived by the cross section of Collins et al. (2008) (see Table 2). b) Selected 20° section to the southwest of the crater center that served as standard for the megablock and Bunte Breccia volume calculations in the entire megablock zone.

Table 3. Classification of the regions outside the Ries impact crater obtained by Sturm et al. (2013).

Region outside the crater	Radius "r" derived after Sturm et al. (2013) (Fig. 5)	Bunte Trümmermassen thickness "t_{BT_out}"
1	18,850	87.67
2	27,560	117.80
3	31,000	51.38

Bunte Trümmermassen thicknesses "t_{BT}," using the block sizes obtained from Sturm et al. (2013), and we calculated the volume of the Bunte Trümmermassen "V_{BT_out}," Bunte Breccia "V_{BB_out}," and of the megablocks "V_{MB_out}" (see Equation 4), respectively. To account for hidden subsurface megablocks, we corrected the number and volumes of megablocks by the factor "s" (see Equation 7).

The volume of Bunte Trümmermassen "V_{BT_out}" for the three regions with different Bunte Trümmermassen thickness values "t_{BT}" of Sturm et al. (2013) for a 180° section south of the crater rim (Fig. 5) is given by:

$$V_{BT_{out}} \sum_{i=1-3} \pi r_{i+1}^2 t_{BT(i+1)} - \pi r_i^2 t_{BT(i+1)} \quad (8)$$

The volume of Bunte Breccia "V_{BB_out}" is determined from the "V_{BT_out}" and "V_{MB_out}."

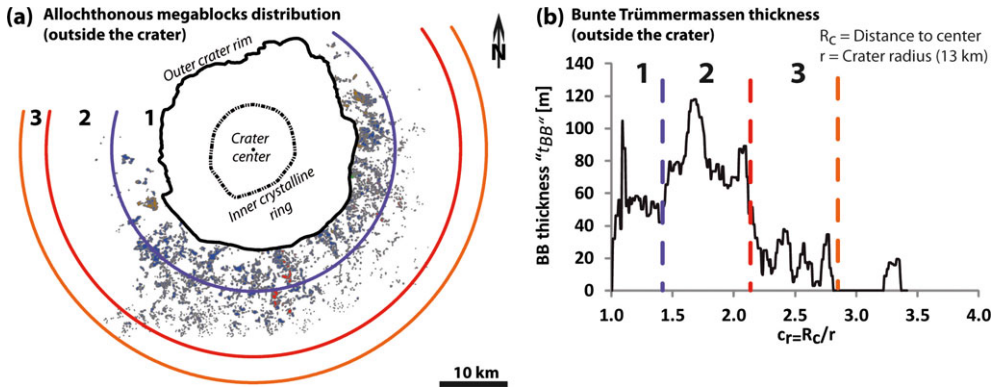

Fig. 5. Sketch illustrating the volume calculations for (a) megablocks and Bunte Trümmermassen outside of the crater. The region outside of the crater is subdivided into three regions with specific Bunte Trümmermassen thicknesses "t_{BT}." Bunte Trümmermassen thicknesses "t_{BT}" are derived using the thickness estimates of Sturm et al. (2013) (see Table 3). b) *X*–*Y* plot of the Bunte Trümmermassen thickness "t_{BT}" variation outside of the Ries impact crater (modified after Sturm et al. 2013).

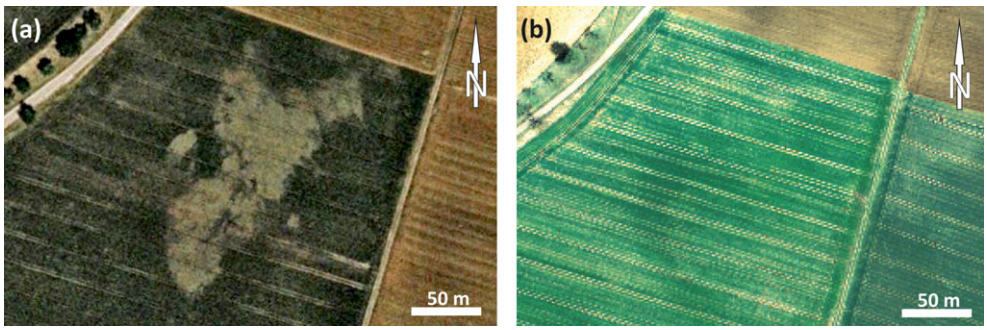

Fig. 6. a) Example of a subsurface crystalline megablock near Marktoffingen, Ries, visible in Google Earth and b) HRSC image of the same region seen in (a), which lacks the subsurface megablock albedo feature.

Sources of Error

The maps of the megablock zone and of the continuous ejecta blanket outside the crater rim are based on remote sensing data, fieldwork, and on the recently revised geologic map of the Ries crater 1:50,000 (Hüttner and Schmidt-Kaler 1999). Different sources of error need to be addressed:

Remote Sensing

The recognition of subsurface megablocks using high-resolution image data sets (e.g., Google Earth and HRSC-AX) is limited due to data resolution, data coverage, and acquisition date. The image data acquired from Google Earth are more useful for the detection of megablocks than the HRSC-AX data, due to their more complete coverage of the crater and favorable vegetation conditions during the time when the images were taken (Fig. 6). Due to different acquisition dates and differences in the cloud cover, varying illumination conditions and image qualities resulted. The detection and visibility of buried megablocks is limited to a depth of approximately 1.5 m below the surface. It is not possible to distinguish different megablock lithologies (e.g., limestone or crystalline) by using remote sensing data sets alone and further characterization of megablocks by shallow drilling is required. The method is restricted to open fields and cannot be used in areas with dense vegetation (e.g., forest), building structures (e.g., villages), or paved roads.

Geologic Map

The current geologic map of the Ries (1:50,000; Hüttner and Schmidt-Kaler 1999) has been assembled from a number of detailed geologic maps (in total 45 geologic maps at the scale of 1:25,000) that were compiled at different times (1924–1994) by different geologists with different working hypotheses. As a consequence, many early maps contain inconsistencies, in particular at the boundaries of neighboring maps. Hüttner and Schmidt-Kaler (1999) reconciled most of these discrepancies and their 1:50,000 scale summary provides a much improved understanding of the occurrence of the Bunte Trümmermassen. The

subdivision into allochthonous and parautochthonous megablocks, however, may still be affected on occasion by possibly erroneous assignments in some of the earlier maps.

Other Causes of Misinterpretations

Some natural features can mimic subsurface megablock structures. (1) The vegetation cover can, in rare cases, look similar to megablock structures (e.g., grain fields with higher albedo features in airborne images). (2) Quaternary deposits, mainly sands, can show a patchy structure that can be misinterpreted as buried megablocks, in particular when the terrane is partially saturated with water. Sands deposited by active and meandering river systems (e.g., Wörnitz) have a similar effect. (3) Anthropogenic activity (e.g., mining, quarrying, or buildings) is likely to mask buried megablock structures.

Also, it can be demonstrated that some Malmian megablocks beyond the morphologic rim represent local materials excavated during ballistic sedimentation, rather than primary crater ejecta. However, suitable criteria to assign each megablock consistently either of these origins are lacking, which is the reason why we followed Hörz et al. (1983) and assigned all Malmian megablocks to primary crater ejecta. There also exist megablocks of Molasse sediments, yet the latter were not mapped in the same detail as the crater-derived megablocks. This is the reason why we could not include these locally excavated megablocks in our detailed analysis.

RESULTS

Improvement of Block Size: Two Case Studies

The Malmian limestone megablock at Hürnheim (Figs. 7 and 8) and the crystalline megablock at Marktoffingen (Figs. 9 and 10) represent two characteristic examples that illustrate the application of our methods to detect subsurface megablock structures.

Hürnheim (10°29′7.1″E/48°37′27.5″N)

This large Malmian limestone megablock is exposed at the surface, but is in contact with a subsurface megablock (Fig. 7a). The exposed megablock encompasses an entire hill and is visible in remote sensing images due to its cover by characteristic vegetation of juniper bushes and low grass. It is approximately 550 m long and approximately 250 m wide and dips to the east. In this area, limestone fieldstones are abundant. The subsurface part of the megablock is approximately 100 m long and up to approximately 70 m wide. Drilling sites D 049 and D 050 are both located directly on the megablock and fragments of the weathered megablock were found at shallow depths of 0.45 m and 0.30 m, respectively (Fig. 7b). D 048 is located next to the megablock, but no limestone material could be found in the uppermost 1.76 m of the ground. Instead, clay and silt material occurred to a depth of 1.40 m.

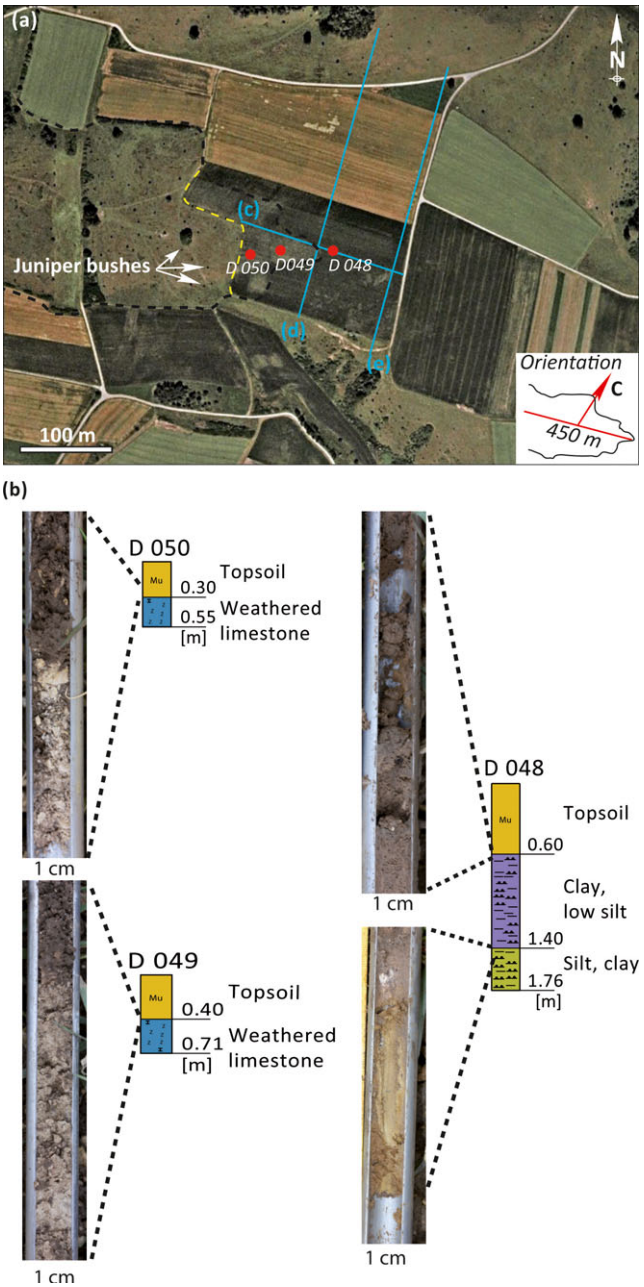

Fig. 7. Case study at Hürnheim, Ries: a) Google Earth image of the Malmian limestone megablock near Hürnheim (right inset illustrates the outline and orientation of the subsurface part of the limestone megablock) and b) core profiles.

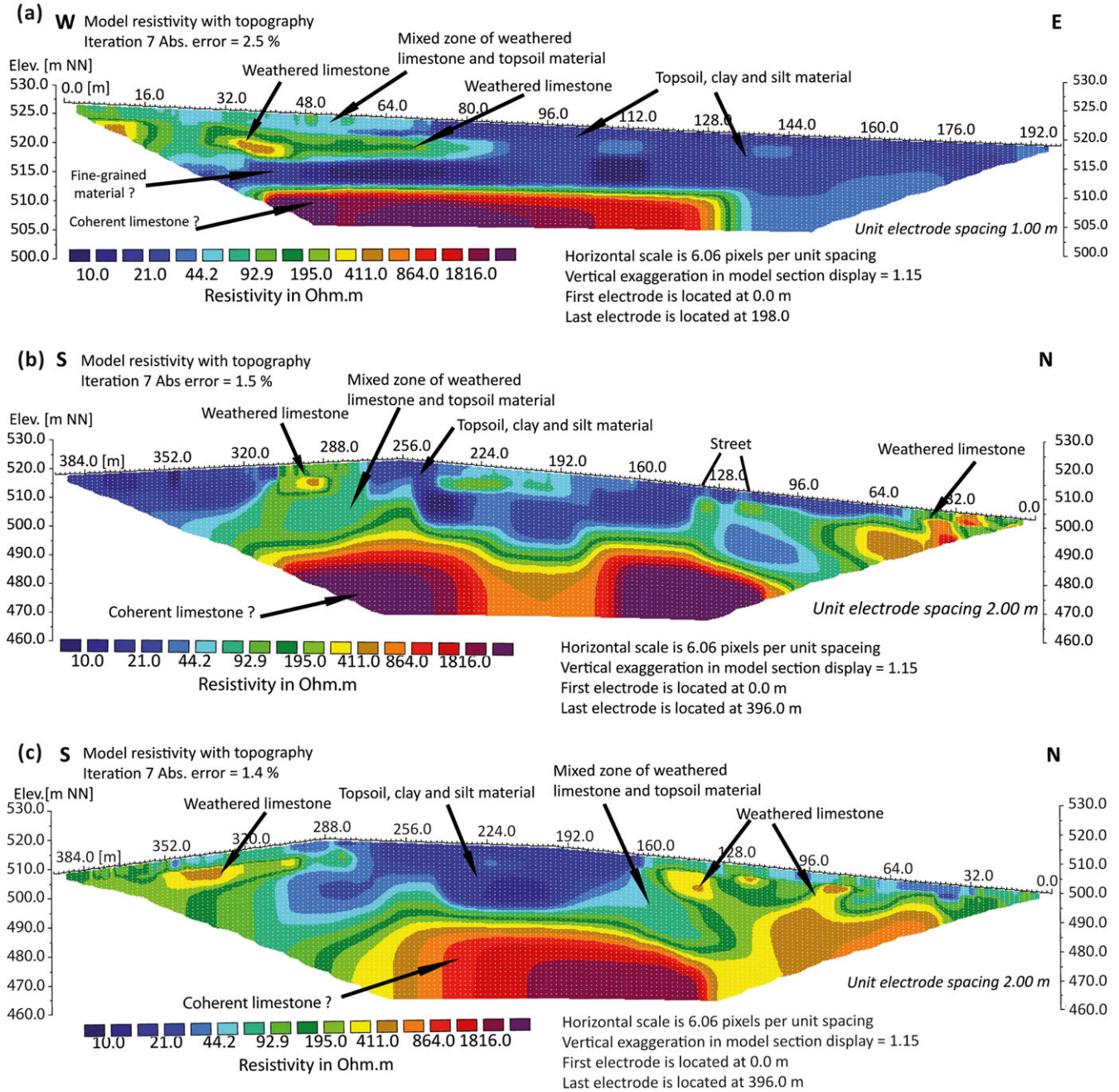

Fig. 8. Geoelectric resistivity measurement profiles of the Hürnheim limestone megablock; locations are shown as blue lines in Fig. 7a (*Abs error* is the root mean square error between the observed apparent and modeled resistivity data).

Figures 8a–c show the modeled resistivity of the field with the subsurface limestone megablock structure. One west–east-trending geoelectric resistivity profile using 1 m unit spacing and two south–north profiles using 2 m unit spacing were acquired to define the size of the megablock at depth. In the west–east-trending profile, the subsurface Malmian limestone megablock is located between 0 and 85 m of the measured profile. The overlying material in the east of between 75 and 192 m depth consists of fine-grained clay and silt material, which causes low resistivities between 10 and 40 Ωm (blue in Fig. 8a). The mixed zone between the surface and the more coherent Malmian limestone material in the subsurface presumably consists of a mixture of clay, silt, and limestone fragments with resistivities between 50 and 200 Ωm (light blue). The

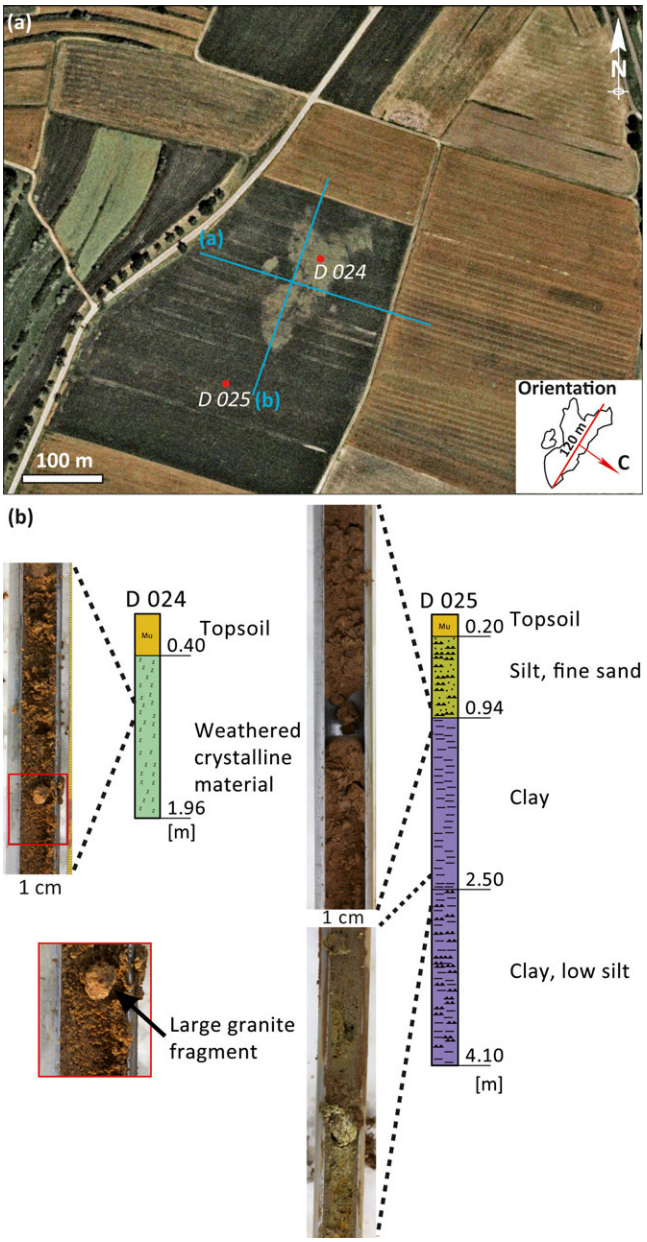

Fig. 9. Case study at Marktoffingen, Ries: a) Google Earth image of a crystalline megablock near Marktoffingen (right inset illustrates the outline and orientation of the subsurface part of the crystalline megablock) and b) core profiles.

underlying material probably consists of more coarse-grained limestone with resistivity values between 100 and 200 Ωm (olive, green). The coarse-grained limestone material represents a subsurface limestone megablock that is covered by up to 8 m clay and silt material between 70 and 90 m of the measured profile. Several parts with higher resistivity values of 400 Ωm (yellow) could represent more coherent parts of the Malmian limestone megablock in the west. However, these higher resistivities could also be caused by a number of smaller limestone blocks. The subsurface megablock is underlain by approximately 8 m thick fine-grained material with resistivities of 10–20 Ωm (blue). Higher resistivity values between 200 and 2000 Ωm (yellow, purple) at a depth of 15 m below the surface could represent the same coherent subsurface limestone megablock that is visible in the north–south profiles at a depth of 20 m below the surface. Ground truth data from analyzing deeper borehole profiles are necessary to verify this interpretation.

In the first south–north profile (Fig. 8d), the observed subsurface Malmian limestone megablock is located between 270 and 300 m and shows resistivity values between 40 and 500 Ωm (green, yellow, brown). The central part of the profile between 60 and 270 m is overlain by fine-grained silt and clay material with resistivities <40 Ωm (blue). In the north, between 0 and 60 m, weathered limestone material with resistivity values between 80 and 800 Ωm is only covered by thin topsoil. The area in the north is cut by a street which is reflected by higher resistivity values between 40 and 100 Ωm (light blue, green).

In the second south–north profile (Fig. 8e), the Malmian limestones are located 5 m below the surface in the southern and northern sections of the profile. They are only covered by thin layers of topsoil, as well as silt and clay material, with resistivities between 40 and 200 Ωm (light blue, green). In the central parts between 160 and 288 m, the structure is overlain by up to 20 m thick, fine-grained clay and silt material with resistivity values between 10 and 20 Ωm (blue). Without ground truth data for the deeper regions with higher resistivity values between 800 and 2000 Ωm (purple) of both south–north profiles, it is not possible to verify the lithology of the subsurface material. The resistivity values for limestone range from 150 Ωm for weathered and wet limestone to 10,000 Ωm for coherent limestone (Table 1). Thus, deeper parts with higher resistivities between 400 and 2000 Ωm (yellow, purple) most likely represent a more coherent limestone megablock 20 m below the surface.

Marktoffingen (10°28′10.9″E/48°45′12.6″N)

The crystalline megablock is visible in Google Earth images as a light gray outline surrounded by a dark vegetation-free field (Fig. 9a). It is approximately 120 m long and approximately 50 m wide and has a nearly tangential orientation of its long axis with respect to the crater center (Fig. 4a; right inset). The local disintegration of the block as well as tensile fractures are readily visible in the satellite image. Drill site D 024 is located directly on the megablock and weathered crystalline material was found at depth of

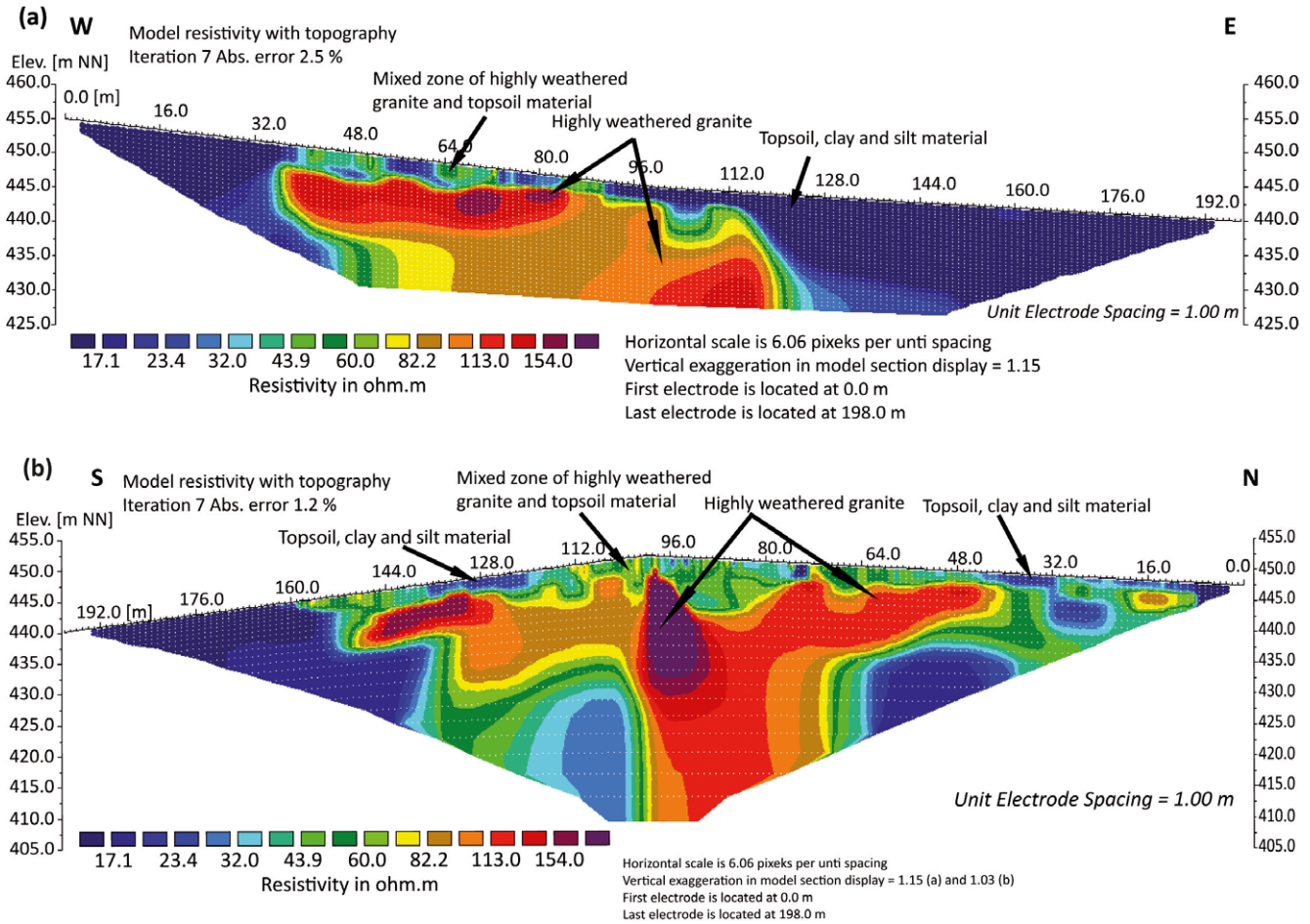

Fig. 10. Geoelectric resistivity measurement profiles of the Marktoffingen crystalline megablock; locations are shown as blue lines in Fig. 9c (*Abs error* is the root mean square error between the observed apparent and modeled resistivity data).

0.40 m (Fig. 9b). The drill site next to the megablock (D 025) did not yield crystalline material down to a depth of 4.10 m, when drilling was stopped. The geologic map shows that the approximate location of the subsurface megablock was already known from fieldstones. Geoelectric resistivity measurements were performed for an east–west profile and a north–south profile, both with 1 m unit spacing (Figs. 10a–b). The overlying material consists of fine-grained clay and silt material, which has low resistivities between 10 and 40 Ωm (blue). The mixed zone presumably consists of a mixture of clay, silt, and highly weathered crystalline material with resistivity values between 40 and 70 Ωm (green). The underlying material to a depth of 5 m from the surface probably consists of more coarse-grained and highly weathered crystalline material of the subsurface megablock with resistivities between 80 and 160 Ωm (yellow, orange, red, and purple). The highly weathered crystalline megablock is located laterally between 35 and 120 m of the measured profile. Figure 10b shows the cross section (north–south profile) of the subsurface crystalline megablock. Compared to the east–west profile, the measured north–south profile shows more irregularly distributed resistivity values over the entire profile. As in the east–west profile, the resistivities for the observed subsurface structure are very low for crystalline rocks (e.g., granites), which should be between 150 Ωm for weathered and wet crystalline and $>10^6$ Ωm for coherent crystalline rocks (Knödel et al. 2005). The observed low resistivities in both cross sections reflect highly fractured and weathered crystalline material in the subsurface, which is consistent with the information from the satellite image.

Distribution of Megablocks

To understand the complex relationship between preimpact target structure and stratigraphy, the crater formation processes, and the postimpact modification, distribution maps and polar plots have been produced for the megablock zone (Figs. 11a and

Table 4. Summary of the number and area of all megablocks of the Ries crater. The megablocks are listed based on their lithology and transport mechanism, "par" refers to parautochthonous and "all" to allochthonous, respectively.

	Total number of megablocks (new identified and megablocks of the geologic map)	Total area (km^2)	Percentages of total area (%)	Mean area (km^2/per block)
Malmian par.	131	22.34	31.63	0.17
Dogger par.	223	22.75	32.21	0.10
Liassic par.	223	13.00	18.41	0.06
Keuper par.	186	12.54	17.75	0.07
All parautochthonous	763	70.63	/	0.09
Malmian all.	2704	109.45	77.88	0.04
Dogger all.	442	13.32	9.48	0.03
Liassic all.	27	0.79	0.56	0.03
Keuper all.	116	3.31	2.36	0.03
Crystalline all.	227	13.67	9.73	0.06
All allochthonous	3289	140.54	/	0.04
Megablocks of unknown stratigraphy	43	0.28		0.01
Total	4095	211.45		0.05

12) and the ejecta blanket outside the crater (Fig. 11b).

Megablock Zone

In general, the allochthonous megablocks show a wider distribution than the parautochthonous blocks, with the latter being concentrated near the crater rim (Fig. 11). The allochthonous blocks excavated from deep and central parts of the inner crater extend from the inner ring to the crater rim, whereas the parautochthonous blocks extend typically no more than 3 km from the final crater rim into the megablock zone, very rarely up to 5 km (Fig. 12). The polar plots illustrate the volumetric distribution of each megablock lithology in the megablock zone (Figs. 12a–f). The parautochthonous Malmian limestone megablocks are concentrated in the SW with smaller and fewer occurrences also present in the SE. All parautochthonous megablocks from lower stratigraphic level in the target are almost missing in this section. Parautochthonous megablocks of Dogger, Liassic, and Keuper age are concentrated in the NW and NE. Large parautochthonous Dogger megablocks are only found in the W and NE and smaller blocks in between these two directions. The parautochthonous Liassic megablocks have a similar distribution. They are also present in the NE, in the region where the crater rim deviates from its otherwise roughly circular form. No parautochthonous Dogger megablocks are present in that region. The parautochthonous Keuper megablocks are present in the sector from NW to NE and their largest area of occurrence is in the NE. Compared to the Dogger and Liassic megablocks, they do not scatter as widely in this sector.

The allochthonous megablocks of Malmian, Dogger, and Keuper lithologies show no preferred azimuthal distribution and are present throughout the entire megablock zone. A minor trend can be recognized for the allochthonous Malmian megablocks, with the largest megablocks found in the SW, SE, and E close to the crater rim. This corresponds to the distribution of parautochthonous Malmian megablocks. The allochthonous Liassic megablocks are too rare for an analysis of their distribution in a statistically meaningful way. Allochthonous crystalline megablocks in the megablock zone are located closer to the crater center and farther from the crater rim than the allochthonous sedimentary megablocks. The largest allochthonous crystalline basement megablocks in the megablock zone are found in the NW and SW (Fig. 12).

Megablocks Outside the Crater

Like the Bunte Breccia deposits, the allochthonous megablocks outside of the Ries impact crater are concentrated from the SW to the east, and are completely eroded in the north. Malmian limestone megablocks represent the most frequent lithology (Table 4; Fig. 11b). The farthest extent of Malmian limestone megablocks is $2.23c_r$ (crater radii) from the crater center. Crystalline basement-derived megablocks show an asymmetric distribution within the megablock zone and outside of the crater and are concentrated in four distinct rays south, southwest, and southeast of the crater, as formerly described by Graup (1978) (Fig. 11b). The farthest extent of crystalline megablocks is $1.92c_r$ from the crater center. Dogger, Keuper, and Liassic megablocks show only minor occurrences in the west and east outside of the crater and the occurrence

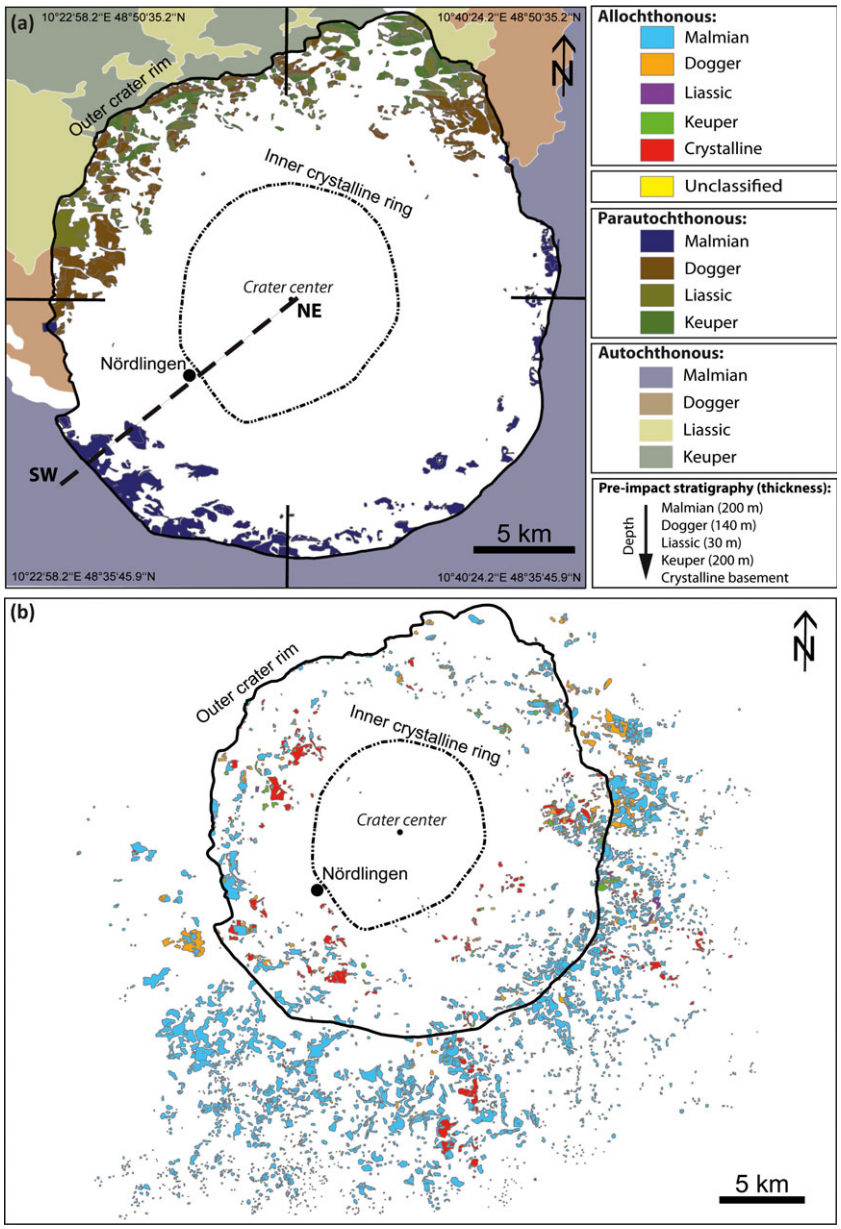

Fig. 11. Distribution of (a) all parautochthonous and (b) all allochthonous megablocks, sorted according to lithologies, in the Ries crater.

extends further to $1.85c_r$, $1.38c_r$, and $1.31c_r$, respectively (Fig. 11b).

Number and Area of Megablocks

We identified 81 new megablock structures in the megablock zone of the Ries. Counting all new and previously known megablocks (Hüttner and Schmidt-Kaler 1999) of the megablock zone and from the ejecta blanket, the total number of megablocks is 4095. The total area of all megablocks is summarized in Table 4 and Figs. 13 and 14. Due to our essentially subsurface survey, the sizes of already known blocks could be corrected, increasing the total area by approximately 1.7 km^2 to a grand total of 211.45 km^2 (Table 4). In summary, there are 763 parautochthonous megablocks with a total area of 70.63 km^2, which represents a mean area of 0.09 km^2/per block and 3289 allochthonous megablocks with a total area of 140.54 km^2, which represents a mean area of 0.04 km^2/per block (Table 4). The higher mean area of the parautochthonous megablocks compared to the

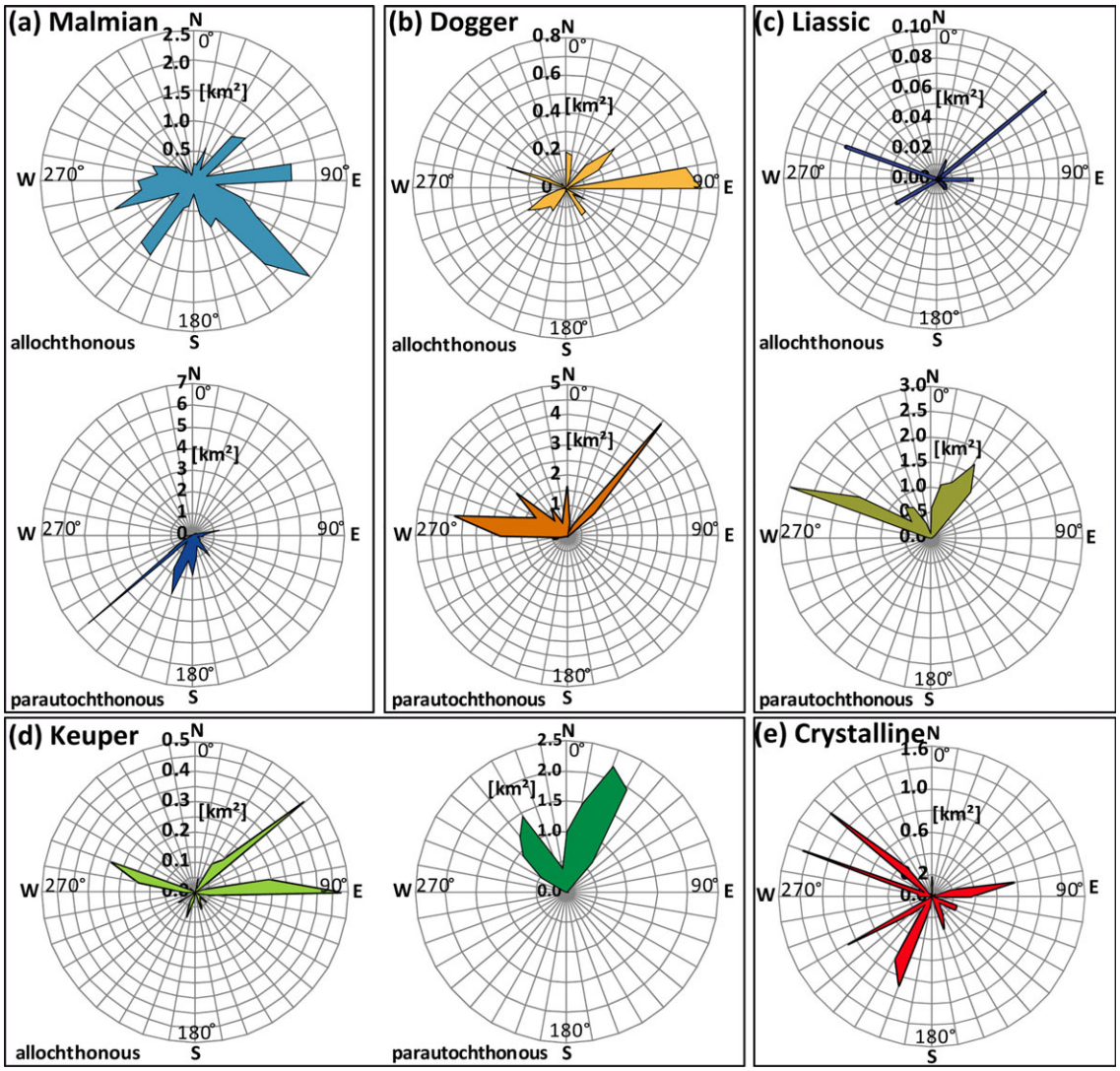

Fig. 12. Polar plots of the area (km^2) occupied in the megablock zone by allochthonous or parautochthonous megablock units at specific azimuths from the Ries crater center.

allochthonous counterparts indicates that the parautochthonous blocks were transported over shorter distances and were less disintegrated and brecciated during crater formation.

Block Size and *D*-values

Outside the final crater rim, all allochthonous sedimentary and crystalline megablocks show a decrease in their total area and mean block size with increasing radial range (Figs. 13, 15, and 16). However, compared to sedimentary megablocks, crystalline megablocks show a smaller decrease in block size with increasing distance from the crater center (Fig. 16).

In the megablock zone, however, the allochthonous megablocks (crystalline and sedimentary) show the opposite trend of area and block sizes with distance (Figs. 13, 15, and 16). All parautochthonous units show an increase in total area and block size with increasing distance from the crater center (Figs. 17 and 18).

Considering all blocks of one particular lithology, the block size distribution obeys a power-law distribution with an exponent *D*. Compared to all allochthonous sedimentary megablocks with a mean *D*-value of −2.278, we derived a smaller *D*-value of −1.65 for crystalline megablocks (Fig. 16). That means fragmentation is pronounced in sedimentary rocks, in particular in clayey Keuper rocks. For the parautochthonous sedimentary units, we derived a mean *D*-value of −1.983 that indicates less fragmentation and stress loading in comparison to the allochthonous counterparts (Fig. 18).

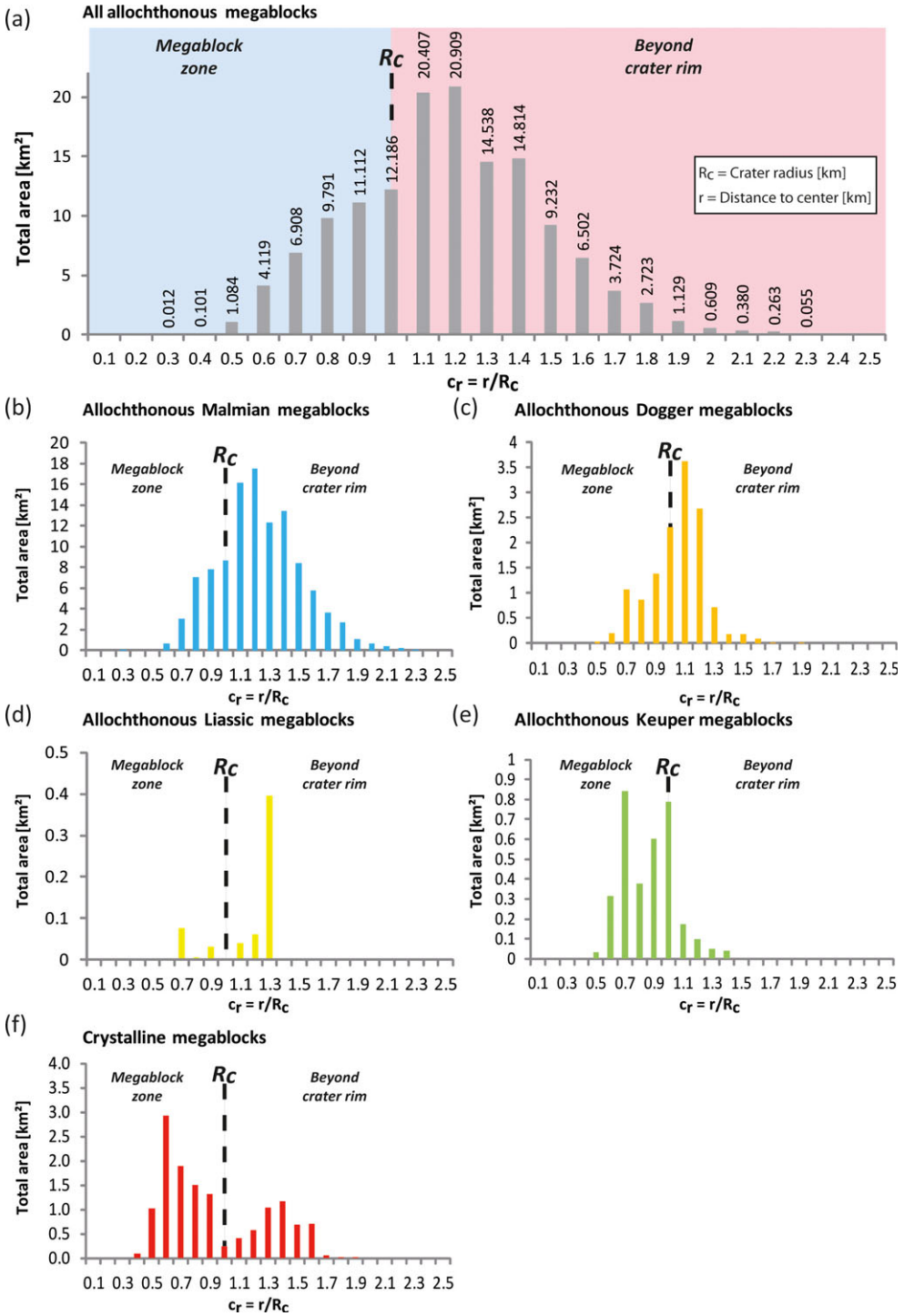

Fig. 13. a) Total area plot of all allochthonous sedimentary and crystalline megablocks versus the distance to the crater center in crater radii (cr), b–e) total area plots of the separated allochthonous sedimentary megablocks versus the distance to the crater center in crater radii (cr), f) total area plot of the crystalline megablocks versus the distance to the crater center in crater radii (cr).

Volumes of Bunte Trümmermassen, Bunte Breccia, and Megablocks

We calculated the volumes of Bunte Trümmermassen "V_{BT}," Bunte Breccia "V_{BB}," and megablocks "V_{MB}" in the megablocks zone (Table 5) and outside the Ries crater (Table 6) applying the procedure described in the Methods section. For the megablock zone, the total volume of Bunte Trümmermassen was estimated to be approximately 63 km^3 and we determined megablock and

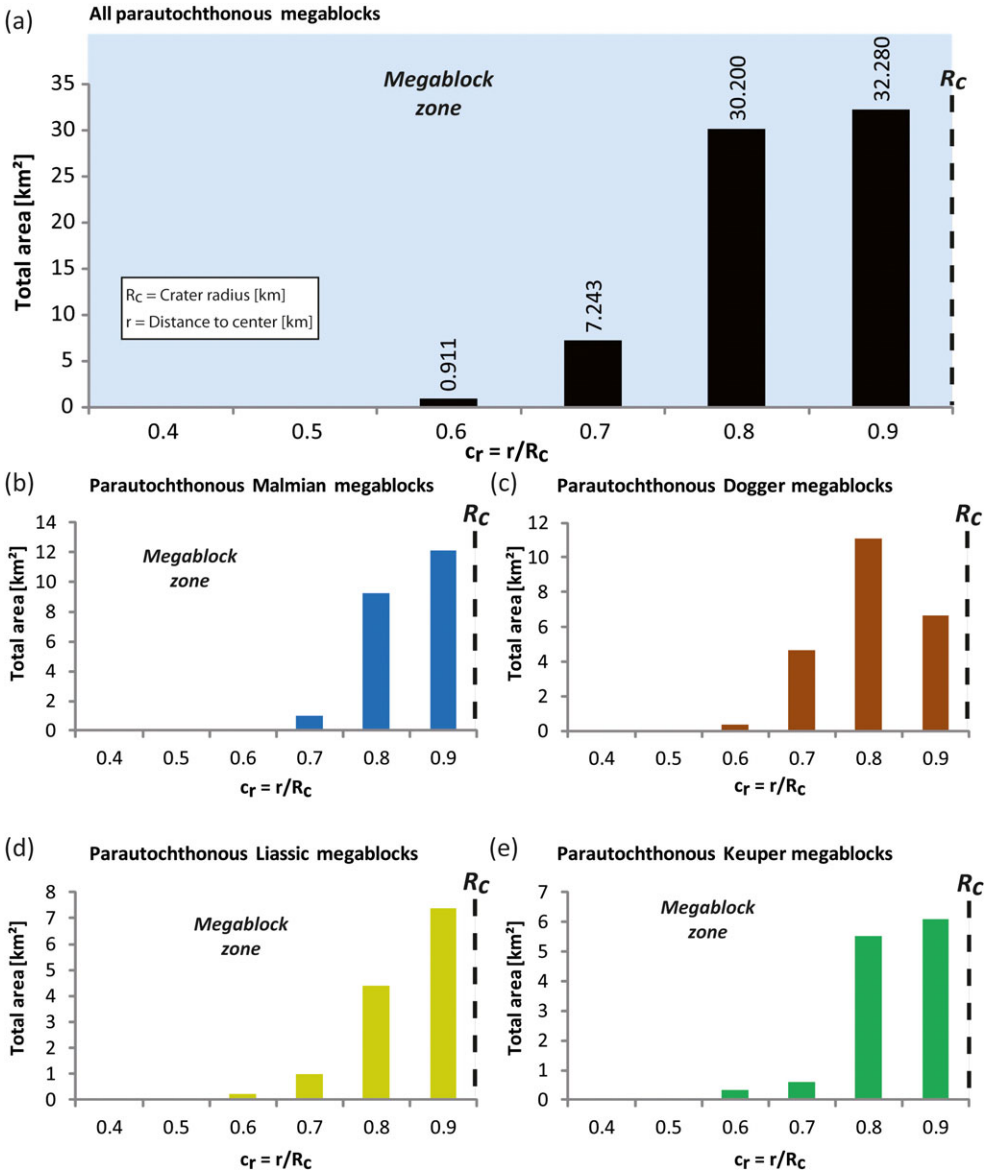

Fig. 14. a) Total area plot of all parautochthonous megablocks versus the distance to the crater center in crater radii (cr); b–e) total area plots of the separated parautochthonous sedimentary megablocks versus the distance to the crater center in crater radii (cr). For parautochthonous megablocks with distances shorter than 13 km from the crater center ($r < 13$ km), the mean crater rim of 13 km was used ($R_c = 13$ km). For parautochthonous megablocks (especially in the north-east section) with distances larger than 13 km from the crater center ($r > 13$ km), the mean crater rim (R_c) was increased to the maximum distance of the crater rim to the crater center ($R_c = 16$ km).

Bunte Breccia volumes of 12 km^3 (19%) and 51 km^3 (81%), respectively (Table 5). For the southern region with the present-day ejecta cover and the eroded northern region outside of the crater, we derived a megablock and Bunte Breccia volume of 35 and 199 km^3, respectively (Table 6). Of these 199 km^3, 44 km^3 of Bunte Breccia are derived from the crater interior; the rest was locally entrained. In total, we obtain 47 km^3 (33%) megablock and 95 km^3 (67%) Bunte Breccia material inside and outside of the Ries impact crater (Table 7).

DISCUSSION

Recognition of Megablocks

Aerial images have the potential to improve the mapping of megablocks of impact craters, even at shallow subsurface levels. A horizontal resolution of approximately 1 m px^{-1} of the remote sensing resources has proven to be sufficient to map subsurface megablocks in great detail. Independent of lithology,

Table 5. Summary of the volume of the Bunte Trümmermassen (V_{BT_in}), megablock (V_{MB_in}), and Bunte Breccia (V_{BB_in}) material situated in the megablock zone of the Ries impact crater (see Fig. 4).

Megablock zone (α = 360°)	Distance range from crater center (m)	BT thickness (m) "t_{BT}" [1] (see Fig. 4)	MB volume (km^3) "V_{MB_in}"	BB volume (km^3) "V_{BB_in}"	BT volume (km^3) "V_{BT_in}"
1	6800–8500	300	2.83	21.68	24.51
2	8500–9500	180	0.33	9.85	10.18
3	9500–11,000	200	5.70	13.62	19.32
4	>11,000	60	3.15	5.90	9.05
Total:			12.02	51.04	63.06

BT = Bunte Trümmermassen, BB = Bunte Breccia, MB = megablocks.
[1] Collins et al. (2008).

Table 6. Summary of the volume calculation of the Bunte Trümmermassen (V_{BT_out}), megablock (V_{MB_out}), and Bunte Breccia (V_{BB_out}) material located outside of the Ries impact crater (see Fig. 5).

Region outside crater (α = 360°)	Distance range from crater center (m)	BT thickness (m) "t_{BT}" [2] (see Fig. 5)	MB volume (km^3) "V_{MB_out}"	BB volume (with secondary material) (km^3) "V_{BB_out}"	BB volume (without secondary material) (km^3) "$V_{BB\_prim\_out}$" [2, 3]	BT volume (without secondary material) (km^3) "V_{BT_out}"
1	13,000–18,850	87.67	21.48	29.84	18.50 (62%)	39.98
2	18,850–27,560	117.80	13.55	136.60	21.86 (16%)	35.41
3	27,560–31,000	51.38	0.10	32.42	3.24 (10%)	3.334
Total			35.13	198.86	43.60	78.72

BT = Bunte Trümmermassen, BB = Bunte Breccia, MB = megablocks.
[2] Sturm et al. (2013), [3] Hörz et al. (1983).

Table 7. Summary of the total volume calculation of the Bunte Trümmermassen (V_{BT}), megablock (V_{MB}), Bunte Breccia (V_{BB}) material of the Ries impact crater.

Total megablock zone + outside crater	MB volume (km^3) "V_{MB}"	BB volume (km^3) "V_{BB}"	BT volume (km^3) "V_{BT}"	Percentage MB (%)	Percentage BB (%)
	47.15	94.64	141.79	33.25	66.75

BT = Bunte Trümmermassen, BB = Bunte Breccia, MB = megablocks.

subsurface megablocks usually appear brighter than their surroundings, and show clearly defined boundaries, mostly in the form of changing vegetation, to their neighboring terrain (Fig. 2). We did not find systematic albedo difference in the remote sensing images for different megablock lithologies and/or depth of the megablocks in the subsurface. Due to albedo contrast, details of the subsurface megablock structures, such as internal fracture networks (Fig. 2c), could even be identified in some cases.

Although in numerous locations at the Ries, subsurface megablocks were previously suspected due to occurrence of specific type of fieldstones, the addition of remote sensing methods provides much clearer and better defined outlines and dimensions of subsurface megablocks.

Volume of Bunte Trümmermassen as a Constraint for the Transient Crater Cavity Size

Our estimate of the volume of Bunte Trümmermassen relies on the correctness of the reconstructed and geophysically constrained cross section through the megablock zone by Collins et al. (2008), and its usefulness as a reference section for the entire megablock zone, as well as the volume calculation of the ejecta blanket outside the crater rim (Sturm et al. 2013). Our calculated volumes for the megablock zone are present-day volumes, yet the amount of erosion would have varied from place to place. It is minimal near the inner crystalline ring, due to a lower topographic high and more erosion-resistant target material (e.g., crystalline basement units), and increases

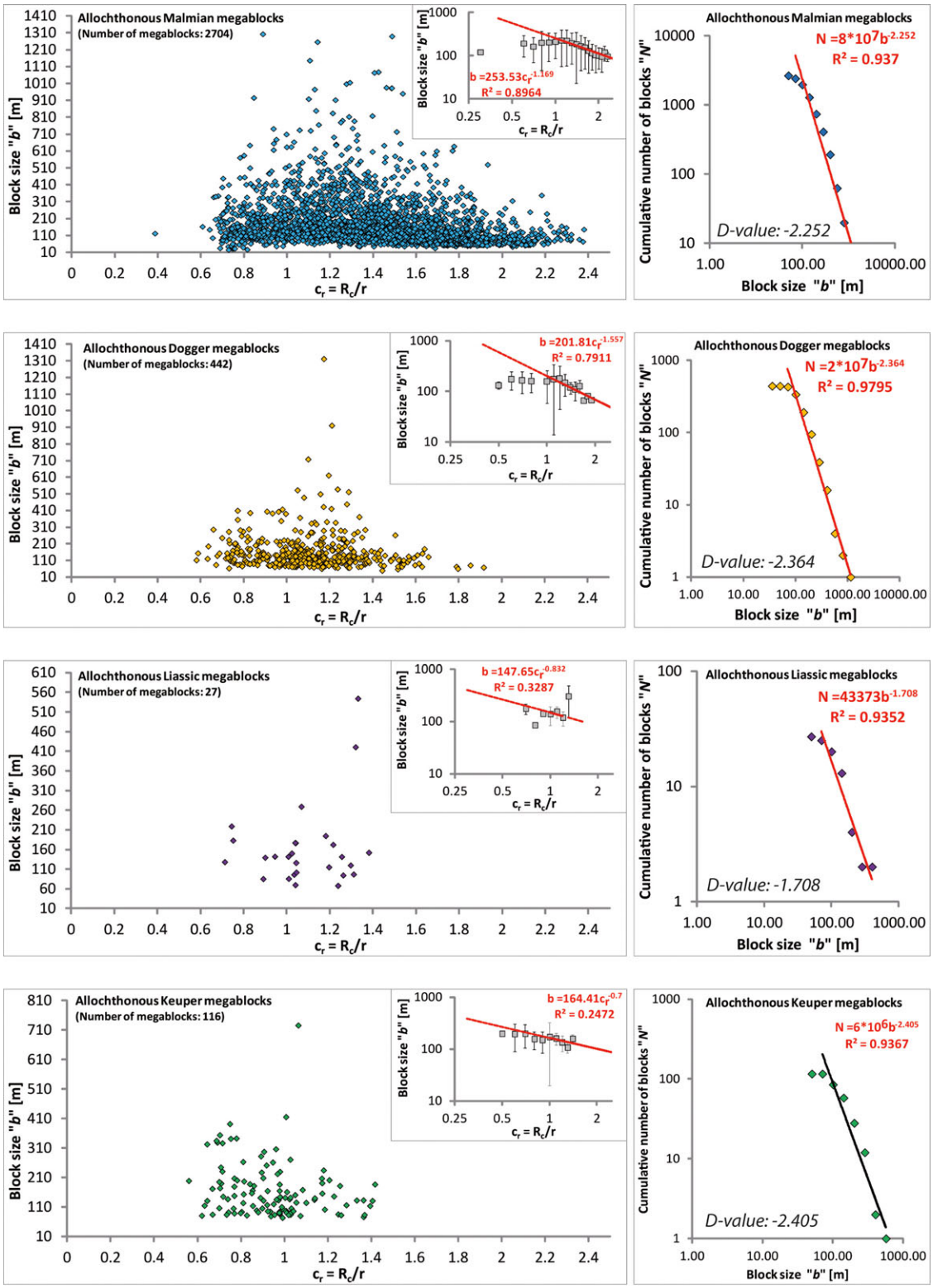

Fig. 15. Left: Block sizes "*b*" of each allochthonous sedimentary megablock structure versus the distance to the crater center in crater radii (c_r). R_c = crater radius (km) and r = distance to crater center (km). Insets: Mean block size "*s*" for 0.1 crater radii (c_r) bins with a derived power-law function (red line) for megablock sizes situated at crater radii larger than 1 ($c_r > 1$). Right: Block size "*s*" versus the cumulative number of blocks "*N*" of a certain size. The derived *D*-values are derived by power-law functions (red line).

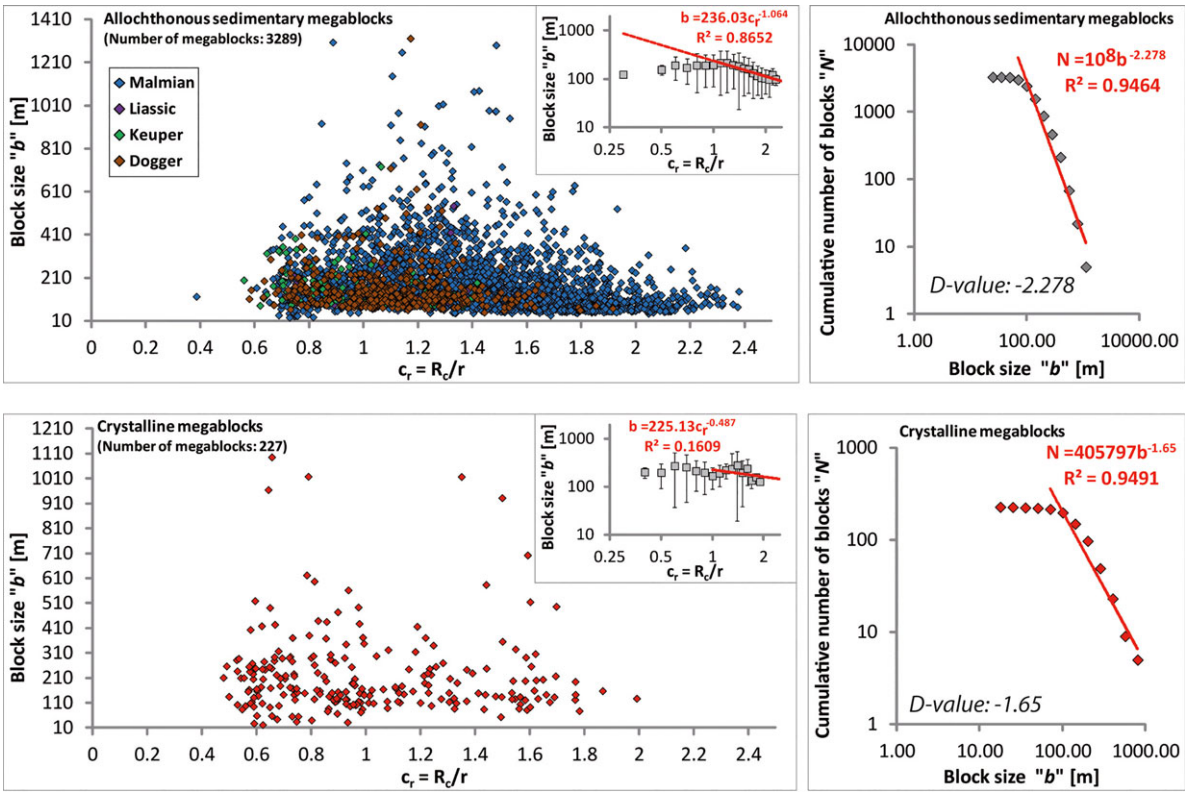

Fig. 16. Left: Block sizes "b" of all allochthonous sedimentary and crystalline megablock structures versus the distance to the crater center in crater radii (c_r). R_c = crater radius (km) and r = distance to crater center (km). Insets: Mean block size "s" for 0.1 crater radii (c_r) bins with a derived power-law function (red line) for megablock sizes situated at crater radii (c_r) larger than 1 ($c_r > 1$). Right: Block size "s" versus the cumulative number of blocks "N" of a certain size. The derived D-values are derived by power-law functions (red line).

toward the final crater rim, a topographic high, where it reaches its maximum. Only locations where the Bunte Trümmermassen are capped by suevite will show the full and original thickness of Bunte Trümmermassen. Locations in the megablock zone that are overlain by suevite and/or deposits of the postimpact Ries Lake can likewise be regarded as nearly pristine with respect to the thickness of the impact deposits. Thus, to determine the volume of erosion, it seems straightforward to superpose onto the present-day topography a plane that is constrained by the elevation of the preserved contacts of Bunte Trümmermassen with either suevite or lake deposits. We estimate on this basis that approximately 22 m of Bunte Trümmermassen is missing, on average, and was eroded in the megablock zone. This adds another approximately 7 km^3 to the calculated volume of Bunte Trümmermassen inside the crater.

In comparison to our total volume estimate of the Bunte Trümmermassen of 149 km^3, Hörz et al. (1983) calculated an ejecta volume of 136 km^3, and Stöffler et al. (2013) derived minimum and maximum volumes of all allochthonous impact formations of 108 and 116 km^3, respectively. The volumes by Stöffler et al. (2013) are corrected for primary and impact-induced porosity and minimum crystalline megablock content. Our volume estimation compares quite well with the volumes derived by Hörz et al. (1983), Stöffler et al. (2013), and with volumes obtained by numerical modeling for the total amount of ejected allochthonous material between 87 and 126 km^3 by Artemieva et al. (2013).

The volume data for Bunte Trümmermassen can be compared with the volume of the transient crater cavity, if we subtract the material that became entrained into the Bunte Trümmermassen upon landing. Hörz et al. (1983) documented that the ejecta blanket at 2.0 crater radii contains up to 90% of locally derived material, whereas at 1.3 crater radii, 38% of the total volume is of local origin. We account for the effect of ballistic sedimentation in the total volume estimate for the area outside the final crater rim (Table 6). For inside the final crater rim, we have assumed that the entity of Bunte Trümmermassen emanated from the transient cavity. For a comparison with the transient cavity volume, we also ought to account for the volume increase that is induced by dilatancy due to

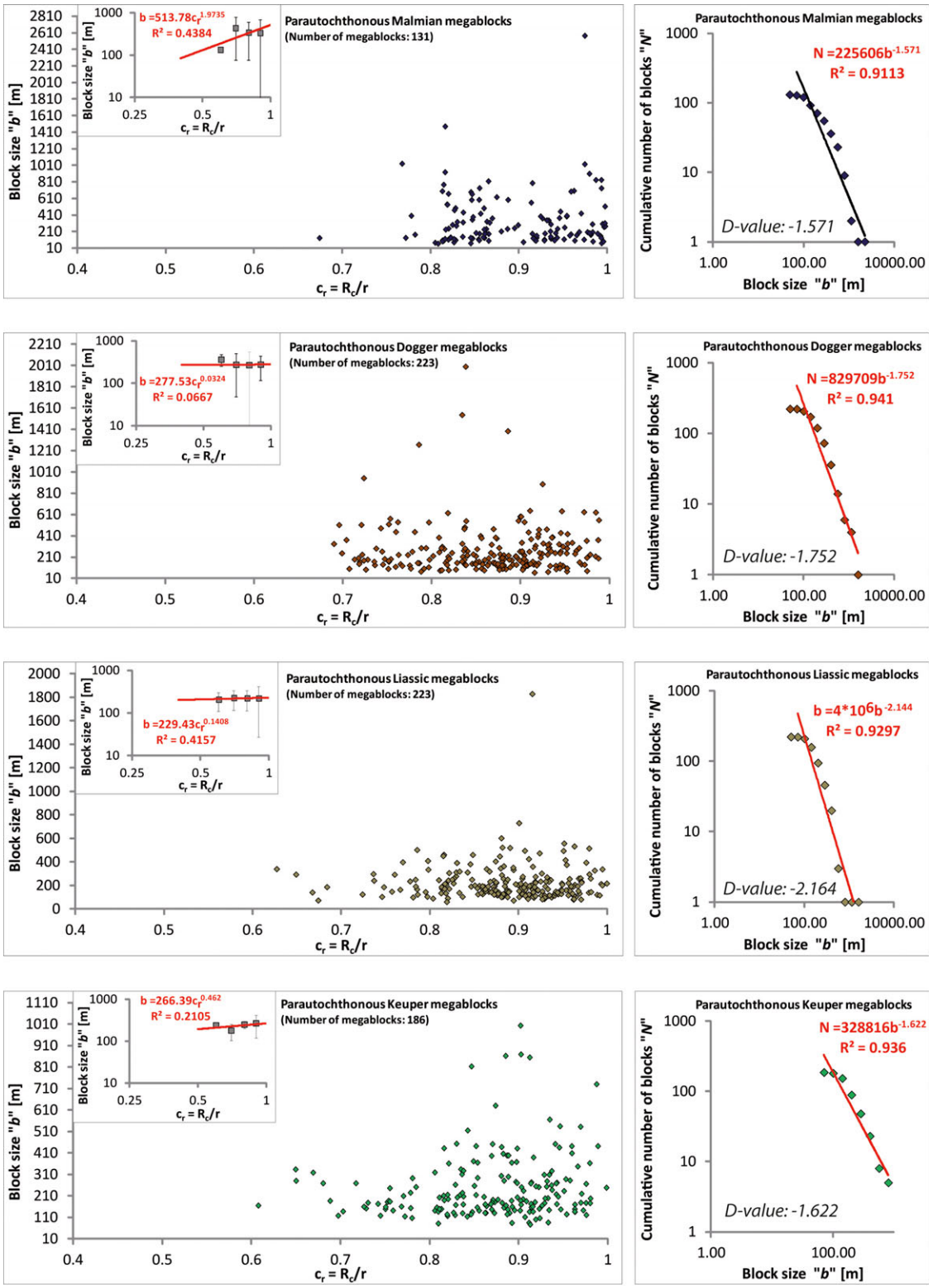

Fig. 17. Left: Block sizes "*b*" of each parautochthonous sedimentary megablock structure versus the distance to the crater center in crater radii (c_r). R_c = crater radius (km) and r = distance to crater center (km). Insets: Mean block size "*s*" for 0.1 crater radii (c_r) bins with a derived power-law function (red line) for megablock sizes situated at crater radii (c_r) smaller than 1 ($c_r < 1$). Right: Block size "*s*" versus the cumulative number of blocks "*N*" of a certain size. The derived *D*-values are derived by power-law functions (red line).

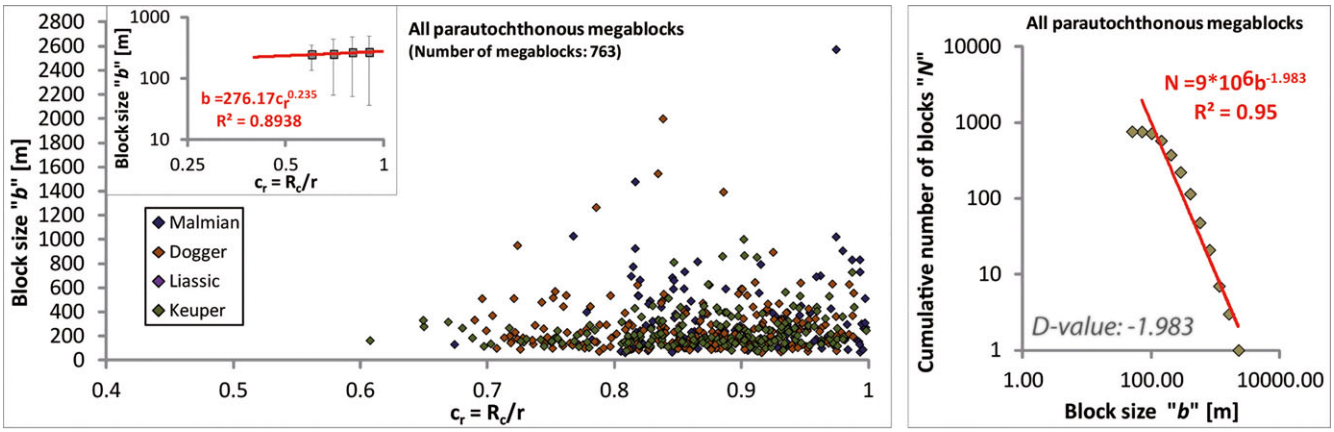

Fig. 18. Left: Block sizes "b" of all parautochthonous sedimentary and crystalline megablock structures versus the distance to the crater center in crater radii (c_r). R_c = crater radius (km) and r = distance to crater center (km). Insets: Mean block size "s" for 0.1 crater radii (c_r) bins with a derived power-law function (red line) for megablock sizes situated at crater radii larger than 1 ($c_r > 1$). Right: Block size "s" versus the cumulative number of blocks "N" of a certain size. The derived D-values are derived by power-law functions (red line).

Table 8. Summary of the transient cavity excavation volumes derived after the method by Croft (1980) using the Maxwell Z-model by Maxwell (1977).

Transient crater radius (km) "r_{tr}"		6.00	7.00	7.50	8.00
Crater depth (km) "c_d"		4.00	4.67	5.00	5.33
Ejection angle (°) "α"		53.13	53.15	53.13	53.12
Parabola volume (km^3) "V_{Tr}"		226.22	358.96	441.73	536.38
Ejected volume (km^3) "V_E"	2.5	64.627	102.625	126.225	153.190
z-values [1, 2]	2.7	85.587	135.909	167.162	202.873
	3.0	113.097	179.594	220.893	268.093

[1] Maxwell (1977); [2] Croft (1980).

fragmentation upon deposition of the Bunte Trümmermassen, but for simplicity in this first-order calculation, we neglect this effect. We used a fixed depth/diameter ratio of the transient cavity of 1/3 (Melosh 1989) and assumed four different maximum transient crater radii "r_{tr}" between 6 and 8 km. The volume of excavation is a fraction of the parabola volume that depends on the shape of the particle trajectories. We applied Maxwell's Z-model (Maxwell 1977) with z-values of 2.5, 2.7, and 3.0 to obtain excavation volumes (Croft 1980) (Table 8).

Assuming an ejection model with $z = 2.7$, as a reasonable overall approximated z-value for the Ries crater (Hörz et al. 1983), the volume of Bunte Trümmermassen suggests a transient cavity size in the order of 14–15 km diameter. In contrast, numerical modeling of the Ries impact by Wünnemann et al. (2005), Collins et al. (2008), and Artemieva et al. (2013) indicated a transient cavity diameter of 9–12 km diameter. There is a general agreement, however, that the present-day crystalline ring of approximately 13 km diameter is the remainder of the transient cavity rim. The cross section of Collins et al. (2008) (Fig. 1) clearly shows that the crater collapse led to extensive normal faulting of the target beyond the transient cavity rim in the area of the megablock zone. Normal faulting disintegrated the target into parautochthonous blocks and accommodated extension perpendicular to the strike of the normal faults. The amount of extension in the cross section of Fig. 1 can be quantified, e.g., by measuring the length of strata in the profile in the undeformed state with respect to the deformed and final state. Using the Dogger to Malmian contact, derived from the profile of Collins et al. (2008), we determine a radial extension of 860 m; the Triassic to Jurassic contact reveals an extension along the cross section of 910 m. An averaged extension of 885 m of the megablock zone implies the same amount of inward shift of the crystalline ring to its present position. Restoring the crater modification, we obtain an initial transient cavity diameter of 13 km + 2*0.885 km = 14.77 km, which is distinctly larger than previous estimates. Thus, restoration and balancing of the deformation of the megablocks on one hand and calculation of the total amount of ejecta (Bunte Trümmermassen) on the other

hand provide two independent lines of evidence that suggest a transient cavity size in the order of 14–15 km diameter.

Distribution of Megablocks

A striking feature in the megablock distribution is the general lack or lesser abundance of megablocks near the crystalline rim (Figs. 14 and 15) up to a 10 km distance from the crater center. This lack is an artifact and is due to the coverage of Bunte Trümmermassen with postimpact Ries Lake deposits. It does not reflect the absence of both parautochthonous and allochthonous megablocks in this area.

As previously outlined, parautochthonous and allochthonous megablocks formed at different stages of the impact process under very different conditions. Allochthonous megablocks moved outward during crater excavation as part of the Bunte Trümmermassen, but originally resided inside the transient cavity. In contrast, the parautochthonous megablocks are fault bounded blocks that moved inward and downward during crater modification. It is, therefore, required to separately discuss the distribution of allochthonous and parautochthonous megablocks.

Parautochthonous Megablocks

Parautochthonous megablocks display a very uneven lithology distribution with Malmian limestone blocks dominating the southern part and being absent in the northern part of the crater. The asymmetric distribution of the parautochthonous megablock lithologies can, in principle, be the result of (1) an oblique impact, (2) stronger erosion by the tributaries of the Rhine in the north compared to the tributaries of the Danube in the south, or (3) the absence of Upper Jurassic strata in the northwestern and northern section of the crater. The uneven occurrences of parautochthonous blocks in the northern and southern sectors cannot be explained by the impact direction, which is most likely from the WSW (Stöffler et al. 2002).

The parautochthonous sedimentary (Malmian, Dogger, Liassic, and Keuper) megablocks show a strong correlation in their distribution and abundance with their occurrence as preimpact host lithologies. Using the distribution maps, the outlines of the lithology-dependent parautochthonous zones can be interpolated to produce an excellent fit to the geologic map (Fig. 11). In this context, the most plausible interpretation for the asymmetric preimpact distribution of the uppermost layer of the sedimentary rocks (Upper Jurassic limestone plateau) is the escarpment crossing the preimpact area of the crater in a WSW–ENE direction. The escarpment had approximately 150 m relief and the Malmian limestone was already eroded in the NW and NE, exposing the underlying Dogger, Liassic, and Keuper units (Pohl et al. 1977; Stöffler and Ostertag 1983).

As shown in the cross section (Fig. 1), parautochthonous megablocks can be regarded as downfaulted blocks, bounded by inward dipping normal faults of straight or listric shape. Both antithetic and synthetic rotations occurred during downfaulting. Strata strike is concentric, on average, which is also expressed in the preferred elongation of blocks tangential with respect to the crater center. Vertical offsets between adjacent blocks may locally reach a few hundred meters. As previously pointed out, normal faulting accommodated approximately 900 m of horizontal extension in radial orientation during crater collapse (Fig. 1).

Previous geoelectrical measurements enabled us to detect and finally distinguish several parautochthonous megablocks near the final crater rim. These units were described as blocks that moved tectonically down- and upward near the final crater rim during crater formation and modification (Homilius and Schmidt-Kaler 1979; Hüttner et al. 1980; Hüttner 1988). Hörz et al. (1983) estimated a volume of 170 km^3 of parautochthonous block masses. However, as the entire target beneath and beside the transient cavity is affected by crater modification movements, a precise definition of a parautochthonous block volume can hardly be given. The decreasing intensity of deformation at increasing distance from the transient cavity gradually reduces the disintegration of the target, so that complete isolation of blocks may gradually die out.

Allochthonous Megablocks

Sedimentary and crystalline allochthonous megablocks are more widely distributed in the crater than the parautochthonous megablocks. The asymmetric distribution of sedimentary bedrock exposed at the preimpact surface is still recognizable, but not as distinct as for parautochthonous megablocks.

The asymmetric, ray-like distribution of the crystalline megablocks with occurrences of brecciated crystalline rocks extending up to distances of 24–27 km from the crater center (Von Engelhardt 1990) may be caused by local highs in the morphology of the crystalline basement (Graup 1978). Based on findings from the Nördlingen drillhole 1973, Stöffler (1977) estimated the total volume of crystalline megablock material to be approximately 30–40 km^3 in the crater. We calculated a megablock volume of all crystalline and sedimentary megablocks of approximately 47 km^3 inside and outside of the crater. Under these

circumstances, our data suggest that this is a slight overestimation for the total volume of crystalline megablocks. From the peripheral and azimuthal distribution of the ejected crystalline megablocks, Graup (1978) developed a model of the original position of the rocks in the basement. In this model, a metamorphic gneiss series is overlain by predominantly granitic units. The crystalline megablocks outside the crater predominantly originate from the uppermost granitic zone of the basement (Graup 1978). The innermost crystalline megablock units (e.g., Wallerstein and Wörnitzostheim) represent remnants of the excavated and uplifted crystalline basement forming the inner crystalline ring. In principle, the inner crystalline ring is build up of an inverted stratigraphy and is described and interpreted as an overturned flap (Dressler and Graup 1974; Pohl et al. 1977). The stratigraphically deeper crystalline basement material was excavated and deposited on top of stratigraphically younger sedimentary units (e.g., Keuper, Liassic, Dogger, and Malmian). This inverted stratigraphy was documented in the Wörnitzostheim drill core (approximately 7.8 km south-east from the crater center) and recently in the Erbisberg drill core obtained southeast of Nördlingen (Dressler and Graup 1974; Pohl et al. 1977; Jung et al. 2011; Kruppa 2013; Wilk 2014). The drill core Wörnitzostheim revealed a sequence of Jurassic and Triassic blocks that are covered by granite and suevite deposits (Förstner 1967; Dressler and Graup 1974; Pohl et al. 1977).

Fragmentation and Megablock Formation during Impact Cratering

The size of megablocks correlates with the overall intensity of deformation of the rock, which—in turn—is a function of the distance to the point of impact. The susceptibility to produce megablocks is a function of (1) the overall strength properties of the particular lithology, (2) the thickness of the strata, (3) the magnitude of the pressure related to the shock front that passed through the particular lithology, and (4) the mode and magnitude of displacement the blocks have suffered.

In general, parautochthonous megablocks are larger compared to their allochthonous counterparts. Parautochthonous megablocks are initially located at greater distances from the crater center, where the shock wave may have already attenuated to a pressure wave. Near-surface spallation (Kenkmann and Ivanov 2006) outside the transient crater plays an important role in the formation of megablocks by creating localized zones of decoupling, most likely along bedding surfaces. These early formed decoupling zones were reactivated during crater modification where the major deformation took place, so that the blocks were finally bounded by faults on all sides. Parautochthonous megablocks are not transported over long distances allowing the megablocks to stay intact. The power-law exponents D of the block size distribution of parautochthonous blocks (Fig. 18) reflect this smaller degree of fragmentation in comparison to that of all allochthonous megablocks. This exponent also varies with lithology, with high D-value characterizing incompetent rock types like claystone and siltstone, and low D-values typical for massive limestone. The presence of weak interbeds is important for the fragmentation behavior. For instance, Malmian limestone occurs in a layered facies in the eastern part of the crater. Here, the bedding planes with thin and soft marly interbeds govern the overall strength of the limestone. These planes of weakness reduce the average block size of Malmian strata in the eastern crater sector with respect to the southern sector where Malmian limestone occurs in a massive reef facies that is devoid of such bedding planes. Incompetent claystones such as the Liassic sedimentary units tend to easily disintegrate during the impact event.

Allochthonous megablocks are more severely fragmented and are more subject to later erosion than parautochthonous megablocks. This is documented by the power-law exponent D of the block size distribution which is -2.28 for the allochthonous units in comparison to -1.98 for the parautochthonous blocks. Again, a lithology dependency exists with low D-values characterizing competent rocks such as crystalline units (D-value -1.65) and high D-values of up to -2.4 typical for clayey materials.

The size of allochthonous megablocks outside the crater decreases with radial distance, which is in accordance with previous measurements (Gall et al. 1977) and models of ejecta emplacement (Oberbeck 1971, 1975; Stöffler 1981; Hörz et al. 1983). This indicates that the distal ejecta emanated from near the transient cavity center, whereas the proximal ejecta originated from regions that were closer to the transient cavity rim. We described the dependencies between allochthonous block sizes and distance to the crater center with power-law distributions. However, these are not very well constrained and are characterized by large scatter. The observed allochthonous megablock distribution in the megablock zone partly disagrees with excavation models of the crater formation process, which implies a decrease in block size with increasing distance from crater center for ejected allochthonous megablocks (Melosh 1989). As mentioned earlier, this deviation mainly results from the postimpact sediment cover near the inner crystalline ring. Allochthonous

megablocks that are not yet detected are mainly expected in the thick pile of Bunte Trümmermasssen near the crystalline ring.

Geologic observations at several impact structures show that the target underneath the transient cavity also disintegrates into megablocks during crater formation (in particular in the central uplift region). Ivanov et al. (1996) determined an average block size of approximately 100 m from the Vorotiv Deep Borehole (5274 m) drilled through the central uplift of the 40 km diameter Puchezh-Katunki impact crater in Russia. Geologic measurements at Upheaval Dome, USA (7 km diameter; Kenkmann et al. 2006) and Waqf as Suwwan, Jordan (6 km diameter; Kenkmann et al. 2010) impact structures revealed block sizes in the range of 50–100 m. The data sets of the two complex impact craters Upheaval Dome and Waqf as Suwwan suggest a trend of increasing block size with increasing distance from the crater center, which is in accordance with theoretical models of rock fragmentation (Grady and Kipp 1987). With the exception of the 1206 m deep research borehole Nördlingen 1973 (FBN73), we have no direct access to the disintegrated, central crater floor of the Ries crater. FBN73 was drilled through approximately 600 m of fragmented crater floor (Stettner 1974). Block sizes of crystalline material range from a few decimeters up to more than 50 m in this borehole (Gudden 1974).

Block sizes determined for the allochthonous megablocks range from 22 to 1322 m, with an average size of 180 m. Parautochthonous megablocks range from 62 to 2574 m, with an average size of 265 m. The allochthonous and parautochthonous block size data obtained from the Ries cannot be directly compared with the block size data obtained from the central uplift material of other craters, because the final block size is further modified by the movement during the excavation process and the final emplacement. Nevertheless, allochthonous and parautochthonous blocks of the Ries show how fragmentation develops with respect to stratigraphic position. Parautochthonous blocks of the Ries were formed adjacent to the transient crater in more distal positions. Thus, the 265 m mean block size is in general accordance to previously published data of block sizes taking into account the more external position of these blocks. Allochthonous blocks, in turn, were formed nearer to the crater center and were consequently ejected. Their size range is remarkable and documents quite plainly the rapidly changing fragmentation conditions during the growth of the transient crater.

With the increasing coverage of high-resolution data, megablocks that were ejected and displaced during the crater formation process are now also known from several lunar and Martian craters (e.g., lunar Aristarchus crater and Martian Martin crater) (Zannetti et al. 2011; Wulf et al. 2012).

CONCLUSIONS

The Ries impact structure is a complex midsized crater and shows characteristic structural zones: A central crater basin bordered by a collar zone of uplifted and overturned, highly faulted blocks (inner crystalline ring) and a so-called megablock zone of large blocks that includes, on one hand, allochthonous megablocks deposited there ballistically as part of the continuous ejecta deposits together with finer grained polymict breccia material (Bunte Breccia) and, on the other hand, parautochthonous megablocks that were displaced during crater collapse.

The distribution of the megablocks in the Ries is controlled by the preimpact geology, the crater formation process, and postimpact erosion. A systematic survey of the megablock zone was performed and a coherent map of the megablock zone was created using a combined approach of aerial image analysis (Google Earth and HRSC-AX) and a field campaign. From this analysis, the following conclusions can be drawn:

The remote sensing detection method in combination with a shallow drilling campaign proved to be successful in finding megablock structures whose upper surface is buried in the upper approximately 1.5 m of the subsurface, as illustrated by the case studies at Hürnheim and Marktoffingen. It is clear that by using this method, not all subsurface megablocks can be detected, as only shallow subsurface megablocks can be observed and vegetation and building structures may inhibit detection. Our systematic survey found 81 new megablocks increasing the total number of megablocks known in the Ries to 4095. For many previously known megablocks, their shape was better constrained and their lithologies verified. As most of the newly found megablocks are relatively small, they added only approximately 1.7 km^2 to the total area of megablocks, which is now approximately 211.45 km^2.

The total volume of ejecta (Bunte Trümmermassen) could be estimated. This volume was used to infer the size of the transient crater cavity which is supposedly larger than suggested previously by numerical modeling. A transient crater cavity of >14.5 km diameter was also determined by balancing the amount of extension in the parautochthonous crater floor of the megablock zone. Volume calculations based on the size measurements of the allochthonous megablocks indicate approximately 12 km^3 of allochthonous megablocks deposited inside the final crater rim and approximately 35 km^3 of allochthonous megablock material outside the crater rim. Parautochthonous megablocks are fewer in number and

larger than their allochthonous counterparts, an indication of their shorter transport and less fragmentation during the modification stage. Allochthonous megablocks are more widely distributed than parautochthonous blocks. Among them, crystalline megablocks occur in rays that extend up to 27 km from the crater center.

Acknowledgments—The drilling equipment was made available by the Institut für Geologie, Westfälische Wilhelms-Universität, Münster and the engineering company Ralf Barfeld in Nördlingen. The geoelectrical equipment was provided by the Landesamt für Umwelt (LfU) of Bavaria. We thank Erwin Geiss and Christian Veress from the Landesamt für Umwelt (LfU) for performing the geophysical measurements and the data processing. The HRSC-AX data were kindly made available by the DLR (German Aerospace Center). The project was partially funded by the Barringer Family Fund. Two grants provided by the German Research Foundation (DFG) to Thomas Kenkmann (Ke 732/19-1 and Ke 732/21-1) allowed us to continue this project. Diligent and very constructive reviews by the two senior experts of the Ries crater, Dieter Stöffler and Fred Hörz, substantially improved the manuscript and stimulated further investigations. We acknowledge the efforts of the associate editor Uwe Reimold.

Editorial Handling—Dr. W. Uwe Reimold

REFERENCES

Abadian M. 1972. Petrographie, Stoßwellenmetamorphose und Entstehung polymikter kristalliner Breccien im Nördlinger Ries. *Contributions to Mineralogy and Petrology* 35:245–262.

Arp G. 2006. Sediments of the Ries Crater Lake (Miocene, Southern Germany). Sediment 2006. Excursion 2. *Schriftenreihe der Deutschen Gesellschaft für Geowissenschaften* 45:213–236.

Arp G., Jung D., and Kenkmann T. 2011. Foschungsbohrung auf miozänem Travertinhügel des Kristallinen Ringes im Nördlinger Ries. *Geoaktiv—Wirtschaft, Beruf, Forschung und Lehre* 45:20–21.

Artemieva N. A., Wünnemann K., Krien F., Reimold W. U., and Stöffler D. 2013. Ries crater and suevite revisited—Observations and modeling, Part II: Modeling. *Meteoritics & Planetary Science* 48:590–627.

Assaad F. A., LaMoreaux J. W., and Hughes T. H. 2004. *Field methods for geologists and hydrogeologists*. Heidelberg: Springer. pp. 70–76.

Bayerisches Geologisches Landesamt, ed. 1969. Das Ries-Geologie, Geophysik und Genese eines Kraters. *Geologica Bavarica* 61:478.

Bayerisches Geologisches Landesamt, ed. 1974. Die Forschungsbohrung Nördlingen 1973. *Geologica Bavarica* 72:98.

Bayerisches Geologisches Landesamt, ed. 1977. Ergebnisse der Ries-Forschungsbohrung 1973: Struktur des Kraters und Entwicklung des Kratersees. *Geologica Bavarica* 75:470.

Brophy K. and Cowley D. 2005. *From the air: Understanding aerial archaeology*. Brimscombe Port: Tempus Publishing Limited. 190 p.

Buchner E., Seyfried H., and van Den Bogaard P. 2003. $^{40}Ar/^{39}Ar$ laser probe age determination confirms the Ries impact crater as the source of glass particles in Graupensand sediments (Grimmelfingen Formation, north Alpine Foreland basin). *International Journal of Earth Sciences (Geologische Rundschau)* 92:1437–3254.

Buchner E., Schwarz W. H., Schmieder M., and Trieloff M. 2010. Establishing a 14.6 ± 0.2 Ma age for the Nördlinger Ries impact (Germany)—A prime example for concordant isotopic ages from various dating materials. *Meteoritics & Planetary Science* 45:662–674.

Collins G. S., Kenkmann T., Osinski G. R., and Wünnemann K. 2008. Mid-sized complex crater formation in mixed crystalline-sedimentary targets: Insights from modeling and observation. *Meteoritics & Planetary Sciences* 43:1955–1977.

Croft S. K. 1980. Cratering flow fields: Implications for the excavation and transient expansion stages of crater formation. Proceedings, 11th Lunar and Planetary Science Conference. pp. 2347–2378.

Di Vincenzo G. and Skala R. 2009. 40Ar–39Ar laser dating of tektites from the Cheb Basin (Czech Republic): Evidence for coevality with moldavites and influence of the dating standard on the age of the Ries impact. *Geochimica et Cosmochimica Acta* 73:493–513.

Dressler B. and Graup G. 1974. Gesteinskundliche Untersuchungen am Suevit der Bohrung Wörnitzostheim I im Nördlinger Ries. *Der Aufschluss* 25:404–411.

Ernstson K. 1974. The structure of the Ries Crater from geoelectric depth soundings. *Journal of Geophysical Research* 40:229–659.

Förstner U. 1967. Petrographische Untersuchung des Suevit aus den Bohrungen Deiningen und Wörnitzostheim im Ries von Nördlingen. *Contributions to Mineralogy and Petrology* 15:281–307.

French B. M. 1998. Traces of catastrophe: A handbook of shock-metamorphic effects in terrestrial meteorite impact structures. LPI Contribution No. 954. Houston, Texas: Lunar and Planetary Institute. 120 p.

Füchtbauer H., von der Brelie G., Dehme R., Förstner U., Gall H., Höfling R., Hoefs J., Hollerbach A., Hufnagel H., Jankowski B., Jung W., Malz H., Mertes H., Rothe P., Salger M., Wehner H., and Wolf M. 1977. Tertiary lake sediments of the Ries, research borehole Nördlingen 1973—A summary. *Geologica Bavarica* 75:13–19.

Gall H., Müller D., and Stöffler D. 1975. Verteilung, Eigenschaften und Entstehung der Auswurfmassen des Impaktkraters Nördlinger Ries. *Geologische Rundschau* 64:915–947.

Gall H., Hüttner R., and Müller D. 1977. Erläuterungen zur Geologischen Karte des Rieses 1:50000. *Geologica Bavarica* 76:191.

Grady D. E. and Kipp M. E. 1987. Dynamic rock fragmentation. In *Mechanics of rock*, edited by Atkinson B. K. San Diego, California: Academic Press. pp. 429–475.

Graup G. 1975. Das Kristallin im Nördlinger Ries: Petrographische Zusammensetzung und Auswurfs mechanismus der kristallinen Trümmermassen, Struktur des kristallinen Untergrundes und Beziehungen zum Moldanubikum. Unpublished Ph.D. thesis, University of Tübingen, Tübingen, Germany. 191 p.

Graup G. 1977. Die Petrographie der kristallinen Gesteine der Forschungsbohrung Nördlingen 1973. *Geologica Bavarica* 75:219–229.

Graup G. 1978. *Das Kristallin im Nördlinger Ries. Petrographische Zusammensetzung und Auswurfsmechanismus der kristallinen Trümmermassen; Struktur des kristallinen Untergrundes und Beziehungen zum Moldanubikum*. Stuttgart: Enke Verlag. 190 p.

Graup G. 1999. Carbonate silicate immiscibility upon impact melting: Ries crater, Germany. *Meteoritics & Planetary Science* 34:425–438.

Grieve R. A. F. 1987. Terrestrial impact structures. *Annual Review of Earth and Planetary Sciences* 15:245–270.

Griffiths D. H. and Barker R. D. 1993. Two-dimensional resistivity imaging and modeling in areas of complex geology. *Journal of Applied Geophysics* 29:211–226.

Gudden H. 1974. Die Forschungsbohrung Nördlingen 1973—Durchführung und erste Befunde. *Geologica Bavarica* 72:11–31.

Homilius J. and Schmidt-Kaler H. 1979. Ein Profil vom Riesrand südlich Wemding in das östliche Vorries nach geoelektrischen Tiefensondierungen. *Geologisches Jahrbuch* 14:3–10.

Hörz F., Ostertag R., and Rainey D. A. 1983. Bunte Breccia of the Ries: Continuous deposits of large impact craters. *Review of Geophysics and Space Physic* 21:1667–1725.

Hüttner R. 1969. Bunte Trümmermassen und Suevit. *Geologica Bavarica* 61:142–200.

Hüttner R. 1988. Zum Bau des südlichen Ries-Kraterrandes. *Jahrbuch Geologisches Landesamt Baden-Württemberg* 30:231–251.

Hüttner R. and Schmidt-Kaler H. 1999. Die Geologische Karte des Rieses 1:50000 (2. überarbeitete Auflage): Erläuterungen zu Erdgeschichte, Bau und Entstehung des Kraters sowie zu den Impaktgesteinen. *Geologica Bavarica* 104:7–76.

Hüttner R., Brost E., Homilius J., and Schmidt-Kaler H. 1980. Struktur des Ries-Kraterrandes auf Grund geoelektrischer Tiefensondierungen. *Geologisches Jahrbuch* 19:95–117.

Ivanov B. A., Kocharyan G. G., Kostuchenko V. N., Kirjakov A. F., and Pevzner L. A. 1996. Puchezh-Katunki impact crater: Preliminary data on recovered core block structure. Proceedings, 27th Lunar and Planetary Science Conference. pp. 589–590.

Jung D., Sturm S., Arp G., Pohl J., and Kenkmann T. 2011. First description of two new borehole profiles from the Ries crater and suevite Ries impact crater, Germany (abstract #5456). *Meteoritics & Planetary Science* 46:A117.

Kenkmann T. and Ivanov B. A. 2006. Target delamination by spallation and ejecta dragging: An example from the Ries crater's periphery. *Earth and Planetary Science Letters* 252:15–29.

Kenkmann T., Jahn A., and Wünnemann K. 2006. "Block size" in a complex impact crater inferred from the Upheaval Dome structure, Utah (abstract #1540). 37th Lunar and Planetary Science Conference. CD-ROM.

Kenkmann T., Reimold W. U., Khirfan M., Salameh E., Khoury H., and Konsul K. 2010. The complex impact crater Jebel Waqf as Suwwan in Jordan: Effects of target heterogeneity and impact obliquity on central uplift formation. In *Large meteorite impacts and planetary evolution IV*, edited by Gibson R. L. and Reimold W. U. GSA Special Paper 465. Boulder, Colorado: Geological Society of America. pp. 471–487.

Kenkmann T., Poelchau M. H., and Wulf G. 2014. Structural geology of impact craters. *Journal of Structural Geology* 62:156–182.

Knödel K., Krummel H., and Lange G. 2005. *Geophysik*. Heidelberg: Springer. pp. 71–100.

Kruppa C. 2013. Stratigraphie und petrographische Beschreibung der kristallinen Gesteine und Brekzien der Forschungsbohrung Erbisberg (Nördlinger Ries). BSc thesis, Museum für Naturkunde Berlin, Germany. 60 p.

Laurenzi M. A., Bigazzi G., Balestrieri M. L., and Bouska V. 2003. 40Ar/40Ar laser probe dating of the Central European tectite-producing impact event. *Meteoritics & Planetary Science* 38:887–893.

Maxwell D. E. 1977. Simple Z model of cratering, ejection and the overturned flap. In *Impact and explosion cratering*, edited by Roddy D. J., Pepin R. O., and Merrill R. B. New York: Pergamon Press. pp. 1003–1008.

McGetchin T. R., Settle M., and Head J. W. 1973. Radial thickness variation in impact crater ejecta: Implications for lunar basin deposits. *Earth and Planetary Science Letters* 20:226–236.

Melosh H. J. 1989. *Impact cratering: A geological process*. New York: Oxford University Press. 245 p.

Neukum G. and the HRSC-Team 2001. *The airborne HRSC-AX cameras: Evaluation of the technical concept and presentation of application results after one year of operations*. Photogrammetric Week 01. Heidelberg: Wichmann Verlag. pp. 117–131.

Oberbeck V. R. 1971. Laboratory simulation of impact cratering with high explosives. *Journal of Geophysical Research* 67:5732–5749.

Oberbeck V. R. 1975. The role of ballistic erosion and sedimentation in lunar stratigraphy. *Journal of Geophysical Research* 13:337–362.

Osinski G. R., Grieve R. A. F., and Spray J. G. 2004. The nature of the groundmass of surficial suevite from the Ries impact structure, Germany, and constraints on its origin. *Meteoritics & Planetary Science* 39:1655–1683.

Pohl J. and Gall H. 1977. Bau und Entstehung des Ries-Kraters. *Geologica Bavarica* 76:159–175.

Pohl J., Stöffler D., Gall H., and Ernstson K. 1977. The Ries impact crater. In *Impact and explosion cratering*, edited by Roddy D. J., Pepin R. O., and Merrill R. B. New York: Pergamon Press. pp. 343–404.

Rocholl A., Ovtcharova M., Schaltegger U., Wijbrans J., Pohl J., Harzhauser M., and Prieto J. 2011. A precise and accurate "astronomical" age of the Ries impact crater Germany: A cautious note on argon dating of impact material (abstract). *Geophysical Research* 13:EGU2011-13322-7, EGU General Assembly, Vienna.

Sammis C. G., King G. C. P., and Biegel R. 1987. The kinematics of gouge deformation. *Pure and Applied Geophysics* 125:777–812.

Schneider M. 1971. Petrologische Untersuchungen der Bunten Breccie im Nördlinger Ries. *Neues Jahrbuch der Mineralogie—Abhandlungen* 114:136–180.

Scholten F. and Gwinner K. 2004. Operational parallel processing in digital photogrammetry—Strategy and results using different multi-line cameras. *International Archives of Photogrammetry and Remote Sensing II/IV* 35:408–413.

Shoemaker E. M. and Chao E. C. T. 1961. New evidence for the impact origin of the Ries Basin, Bavaria, Germany. *Journal of Geophysical Research* 66:3371–3378.

Stettner G. 1974. Das Grundgebirge in der Forschungsbohrung Nördlingen 1973 im regionalen Rahmen und seine Veränderung durch den Impakt. *Geologica Bavarica* 72:35–51.

Stöffler D. 1977. Research drilling Nördlingen 1973: Polymict breccias, crater basement, and cratering model of the Ries impact structure. *Geologica Bavarica* 75: 443–458.

Stöffler D. 1981. Cratering mechanics: Data from terrestrial and experimental craters and implications for the Apollo 16 site. In: *Workshop on Apollo 16*, edited by James O. B. and Hörz F. LPI Technical Report 81-01. Houston, Texas: Lunar and Planetary Institute. pp. 132–141.

Stöffler D. and Ostertag R. 1983. The Ries impact crater. *Fortschritte der Mineralogie* 61:71–116.

Stöffler D., Artemieva N. A., and Pierazzo E. 2002. Modeling the Ries-Steinheim impact event and the formation of the moldavite strewn field. *Meteoritics & Planetary Science* 37:1893–1907.

Stöffler D., Reimold W. U., Jacob J., Hansen B. K., Summerson I. A. T., Artemieva N. A., and Wünnemann K. 2013. Ries crater and suevite revisited—Observations and modeling, Part I: Observations. *Meteoritics & Planetary Science* 48:515–589.

Sturm S. 2011. Distribution of megablocks in the Ries crater, Germany: Implications for complex craters in the solar system from remote sensing and field analyses. MSc thesis, University of Muenster, Germany. 199 p.

Sturm S., Wulf G., Jung D., and Kenkmann T. 2013. The Ries impact, a double-layer rampart crater on Earth. *Geology* 41:531–534.

Svensson H. 1973. Distribution and chronology of relict polygon patterns on the Laholm Plain, the Swedish West Coast. *Geografiska Annaler* 55:159–179.

Von Engelhardt W. 1990. Distribution, petrography and shock metamorphism of the ejecta of the Ries crater in Germany: A review. *Tectonophysics* 171:259–273.

Von Engelhardt W., Stöffler D., and Schneider W. 1969. Petrologische Untersuchung im Ries. *Geologica Bavarica* 61:229–295.

Wilk J. 2014. Petrography of the Erbisberg drilling in the Ries impact crater. MSc thesis, University of Freiburg, Germany. 160 p.

Willmes M. 2011. Remote sensing and field analysis of the Ries crater, Germany: Distribution of megablocks and mechanical implications for cratering processes in the solar system. MSc thesis, University of Muenster, Germany. 165 p.

Wulf G., Poelchau M. H., and Kenkmann T. 2012. Structural asymmetry in martian impact craters as an indicator for an impact trajectory. *Icarus* 220:194–204.

Wünnemann K., Morgan J. V., and Jödicke H. 2005. Is Ries crater typical for its size? An analysis based upon old and new geophysical data and numerical modeling. *GSA Special Paper* 384:67–83.

Zannetti M., Hiesinger H., dervan Bogert C. H., and Jolliff B. L. 2011. Observation of stratified ejecta blocks at Archistarchus crater (abstract #2262). 42nd Lunar and Planetary Science Conference. CD-ROM.